



# AEC Computing and Applied Mathematics Center

## AEC RESEARCH AND DEVELOPMENT REPORT

PHYSICS  
TID-4500  
14th Ed.

NYO-2877

EXPERIMENTS ON SUPERSONIC PLASMA  
FLOW ALONG MAGNETIC FIELDS. II.

by

David M. Wetstone

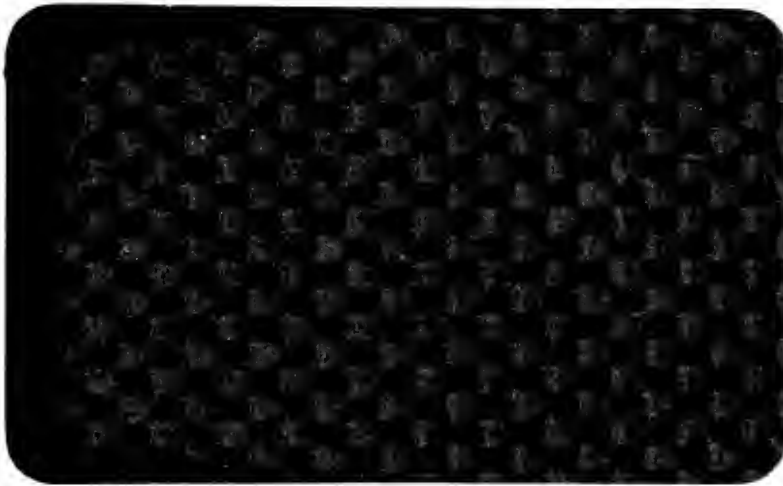
September 30, 1959

---

## Institute of Mathematical Sciences

NEW YORK UNIVERSITY

NEW YORK, NEW YORK



This report was prepared as an account of Government sponsored work. Neither the United States, nor the Commission, nor any person acting on behalf of the Commission:

- A. Makes any warranty or representation, express or implied, with respect to the accuracy, completeness, or usefulness of the information contained in this report, or that the use of any information, apparatus, method, or process disclosed in this report may not infringe privately owned rights; or
- B. Assumes any liabilities with respect to the use of, or for damages resulting from the use of any information, apparatus, method, or process disclosed in this report.



As used in the above, "person acting on behalf of the Commission" includes any employee or contractor of the Commission, or employee of such contractor, to the extent that such employee or contractor of the Commission, or employee of such contractor prepares, disseminates, or provides access to, any information pursuant to his employment or contract with the Commission, or his employment with such contractor.

UNCLASSIFIED

AEC COMPUTING AND APPLIED MATHEMATICS CENTER  
Institute of Mathematical Sciences  
New York University

PHYSICS  
TID-4500  
14th Ed.

NYO-2877

EXPERIMENTS ON SUPERSONIC PLASMA  
FLOW ALONG MAGNETIC FIELDS. II.

by

David M. Wetstone

September 30, 1959

UNCLASSIFIED



# ABSTRACT

Time-integrated photographs are presented of collimated plasma flow parallel to magnetic fields up to 3 weber/m<sup>2</sup>, into and out of magnetic mirrors, and along curved fields. The material projected along the field lines was substantially Cu plasma, created by short vacuum spark bursts (plasmoids), and injected into a vacuum chamber. Non-uniform solenoids expanded or compressed the plasma flow, which followed the field lines. In the case of curved fields, more complicated flows were observed, due to the presence of internal polarization fields, and the plasmoid followed the field lines only when the density (up to  $3 \times 10^{15}$  ions/cc) was sufficiently reduced. Photomultiplier studies were employed with some geometries to estimate center-of-mass and expansion velocities which reached 5.5 and 1.9 cm/ $\mu$ sec, respectively, adequately demonstrating supersonic flow. The latter figure gives an upper bound to ion temperature of 120 eV for Cu. This ion energy is considerably higher than those normally encountered in spark channels and is a substantial fraction (0.12) of the axial energy. A mechanism is described for achieving such thermal energies through the interaction of a strong shock wave with the initial discharge channel,



thermalizing a large fraction of the axial energy. The upper bound for ion Larmor radius was that of the plasma flow. Estimates are presented of electron temperature and degree of ionization. A theoretical total reflection coefficient is derived for a plasmoid entering a magnetic mirror. An experimental transverse drift velocity of  $5 \times 10^4$  cm/sec (in the straight solenoid) is observed and discussed. In the Appendices a complete description is included of the experimental equipment and electrical circuits, and a digital machine computation method is described for obtaining field line distribution and density in a wide variety of coil geometries.





## PERSONNEL AND ACKNOWLEDGMENTS

This project, a part of the Project Sherwood program at New York University, was under the general supervision of Professor Harold Grad, Institute of Mathematical Sciences, and extended over the period of February 1956 through June 1959.

This present, and final, report deals largely with work performed since April 1958.

The project was conceived and initiated by Professor David Finkelstein, who was its director until July 1958; his contributions to the preparation of this report are gratefully acknowledged.

Members of the Institute of Mathematical Sciences, New York University, who have contributed directly to the project are:

Melvin P. Ehrlich, Assistant Research Scientist, May 1956  
to August 1958  
Peter Kerwin, Engineer, February 1956 to February 1958  
Iren Livingston, Technician, September 1956 to September  
1958  
John McNally, Technician, September 1958 to July 1959  
David M. Wetstone, Associate Research Scientist, December  
1956 to July 1959.

The author wishes to acknowledge with considerable appreciation the highly informative conversations he held with Dr. Reimar Lüst (Max Planck Institute for Physics, Munich) which contributed to parts of the theoretical discussion.

The assistance of Mr. Carl Bass, of the Institute, in the preparation of many of the diagrams is gratefully acknowledged.



# TABLE OF CONTENTS

	Page
Abstract . . . . .	2
Personnel and Acknowledgments. . . . .	4
Table of Figures . . . . .	7
I. Introduction . . . . .	9
II. Experimental Procedures and Theory	
A. General Description . . . . .	11
B. Creation of Plasmoids . . . . .	12
C. Creation of Axial Magnetic Field. . . . .	15
D. Firing Synchronization. . . . .	16
E. The Differential Solenoid . . . . .	16
1. Normal Differential Solenoid. . . . .	18
2. Shorted Differential Solenoid . . . . .	26
F. The Curved Solenoid . . . . .	30
G. Center-of-Mass and Expansion Velocity Measurements. . . . .	35
III. Results and Discussion	
A. General. . . . .	37
B. Plasmoid Flow in the Normal Differential Solenoid . . . . .	37
1. Photographic Results. . . . .	38
2. Photomultiplier Measurements. . . . .	46
3. Derived Results . . . . .	55
C. Plasmoid Flow in the Shorted Differential Solenoid. . . . .	76
D. Plasmoid Flow in the Curved Solenoid. . . . .	77



	Page
Appendix I: Experimental Equipment . . . . .	87
Appendix II: Coaxial Plasma Source. . . . .	93
Appendix III: Button Source Trigger. . . . .	94
Appendix IV: Laboratory Designed Circuits . . . . .	97
Appendix V: Photomultiplier Experiment . . . . .	104
Appendix VI: Determination of Flux Distribution in Multiple Circular Coils with Axial Symmetry . . . . .	107
References . . . . .	111



# TABLE OF FIGURES

	Page
1. Schematic of Plasma Source with Differential Solenoid . . . . .	13
2. Schematic of Plasma Source with Curved Solenoid. . . . .	14
3. Light Signal from Plasma Source Mouth. . . . .	17
4. Ringing of Plasma Source and Capacitor Assembly. . . . .	17
5. Flux Line Pattern in Normal Differential Solenoid. . . . .	20
6. Two-Turn Search Coil on Normal Differential Solenoid . . . . .	21
7. Flux Line Pattern in Shorted Differential Solenoid . . . . .	28
8. Two-Turn Search Coil on Shorted Differential Solenoid. . . . .	29
9. Flux Line Pattern in Curved Solenoid . . . . .	32
10. Two-Turn Search Coil on Curved Solenoid. . . . .	33
11. Plasmoid Flow in the Normal Differential Solenoid. I . . . . .	40
12. Plasmoid Flow in the Normal Differential Solenoid.II. Study of Camera Interpretation . . . . .	41
13. Plasmoid Flow in the Normal Differential Solenoid.III. Effect of Field Variation. . . . .	43
14. Plasmoid Flow in the Normal Differential Solenoid.IV. Effect of Field Variation in Closeup . . . . .	44
15. Plasmoid Flow in the Normal Differential Solenoid. V. Diverting of Plasma Filament . . . . .	47
16. Plasmoid Flow vs. Flux Line Behavior at a Magnetic Mirror . . . . .	48
17. Photomultiplier Traces of Plasmoid Transit without Field. . . . .	49
18. Photomultiplier Traces of Plasmoid Transit with Field. . . . .	52
19. Effectiveness of Magnetic Mirror for Variation of Particle Velocity Orientation in Moving Plasmoid . . . . .	73





20.	Plasmoid Flow in the Shorted Differential Solenoid, I. Single Jumper . . . . .	78
21.	Plasmoid Flow in the Shorted Differential Solenoid, II. Double Jumper . . . . .	79
22.	Plasmoid Flow in the Curved Solenoid. I. Plasmoid at 40 Joules . . . . .	80
23.	Plasmoid Flow in the Curved Solenoid. II. Plasmoid at 10 Joules. . . . .	83
24.	Plasmoid Flow in the Curved Solenoid. III. Plasmoid at 2.5 Joules . . . . .	84
25.	Experimental Arrangement with Differential Solenoid . .	89
26.	Button Source Trigger . . . . .	90
27.	Experimental Arrangement with Curved Solenoid . . . . .	91
28.	Schematic of System . . . . .	92
29.	Detail of Coaxial Plasma Source . . . . .	95
30.	Detail of Spark Gap Trigger . . . . .	96
31.	Pulse Amplifier Circuit . . . . .	99
32.	Main Power Supply Circuit . . . . .	100
33.	Ignitron Unit Circuit . . . . .	101
34.	Control Unit Circuit. . . . .	102
35.	Meter Relay Circuit . . . . .	105



## EXPERIMENTS ON SUPERSONIC PLASMA FLOW ALONG MAGNETIC FIELDS. II.

I. Introduction

This report presents the continuation of the work first described in 1958<sup>1</sup> on the motion of plasmoids along diverted magnetic field lines, and is the major and final report.

Recently, the experimental applications of plasma physics have been largely the controlled thermonuclear fusion problem, wherein almost all approaches have utilized some form of static plasma, either self-contained or with a superimposed magnetic field, or both.<sup>2</sup> The experiments reported here differ in that an individual burst of plasma (plasmoid) is projected into an evacuated chamber and subjected to various magnetic field geometries. However, this present work was not directed toward the attainment of fusion but was motivated primarily by the desire to investigate a relatively new kind of phenomenon and gain qualitative, and some quantitative, information which might serve to suggest and encourage research in this direction of plasma physics.

Some fundamental questions asked were, will a uniform  $B_z$  field collimate plasmoid flow, and over what distance? What would be the behavior of a projected plasmoid in regions of converging field lines (magnetic mirror), diverging field lines, or curving field lines? How do the center-of-mass and thermal velocities of the plasmoid behave under these conditions? Some of these questions have already been examined in the first report,<sup>1</sup> and others are undertaken here.

Interest in plasmoids is largely associated with Bostick<sup>3,4</sup> who has described a "button" or "rail" source for their generation and propulsion across magnetic fields, and has given considerable thought to the morphology of the plasmoid, itself. This work was continued by Finkelstein, et al.,<sup>5</sup> who designed and initiated the presently reported program.

There are several other investigations in which plasmoids were shot into magnetic fields or were magnetically accelerated. Sinelnikov, et al.,<sup>6</sup> employed magnetic and electron probes to detect the radial polarization of a plasmoid when entering an axial magnetic field, a variety of plasmoid was transferred and compressed in stages by Coensgen<sup>7</sup> in a fusion device at Livermore called Toy Top, and experiments were recently reported by Marshall,<sup>8</sup> utilizing the technique of a traveling magnetic wave to compress a plasmoid and accelerate it into a vacuum region.

To date, there has been no published attempt to guide a plasmoid around a curved field, as has been tried here, though there are a number of examples of sustained, curved discharges. One of the more interesting of these is the  $180^\circ$  plasma beam photographed by Harrison and Dawton<sup>9</sup> at Harwell, which was stabilized by axial magnetic fields.

It is hoped that the broad survey of phenomena, investigated and described so briefly herein and in the previous report, will serve to encourage further investigations in this interesting subject.

## II. Experimental Procedures and Theory

A. General Description: The phenomenon studied was the behavior of a plasmoid produced by a vacuum spark discharge which was injected along magnetic field lines which were diverted or curved, all within an evacuated tube. In most cases observations were made on individual discharges (shots), although there were indications that a single shot may have consisted of a number of individual sub-bursts, due to capacitor ringing, which fused into a single plasmoid during passage along the tube.

The plasma was created by the high-speed discharge of a capacitor across a coaxial source (see B, below). The magnetic field was created by the discharge of a capacitor bank (see C, below) across a suitable solenoid around a cylindrical glass tube, the plasma being injected axially at one end. The fields reached maximum relatively slowly (the order of 100 to 150  $\mu\text{sec}$ ), while the plasmoid was created and traversed the tube rapidly (the order of 10  $\mu\text{sec}$ ). Thus, the plasmoid saw an approximately D. C. field. It was necessary to employ a synchronization system to achieve this effect (see D, below). The vacuum equipment (see Appendix I) maintained the pressure in the range of  $3 \times 10^{-6}$  to  $8 \times 10^{-6}$  mm Hg, except during the first few seconds after each shot, but shots were spaced at least one minute apart.

Two types of solenoids and tubes were employed. The first was a straight helix of constant diameter, of which the center portion was wound with smaller pitch than the ends (see B, below); this helix was placed around a straight cylindrical glass tube. Most of the observations reported herein employed

this geometry. A variation was obtained by shorting (and cutting) the center section. The second arrangement employed a uniform curved helix of constant diameter, fitted around a curved cylindrical glass tube (see F, below).

The bulk of the observations consisted of time-integrated photographs of individual plasmoid shots traversing the tube, over a wide range of photographic conditions and positions, employing Polaroid 46L film. In addition, one geometry was utilized to make an extensive study of plasmoid center-of-mass and expansion velocities, employing the photomultiplier technique (see G, below).

As will be noted, the details of the experimental equipment will be found in various parts of the Appendices.

B. Creation of Plasmoids: The plasmoids were created by a vacuum spark discharge across a coaxial source used in conjunction with a low-inductance capacitor. Mechanical details of the system will be found in Appendix II. The capacitor was rated at  $0.55 \mu\text{F}$  and  $0.040 \mu\text{h}$ , and was fired at 8, 12, and 16 kV. However, unless otherwise stated, firing was at 12 kV, producing about 40 joules.

The plasma source was positioned coaxially at one end of the tube and solenoid, the positioning being somewhat different for each of the two solenoid geometries employed. These two arrangements are shown schematically in Figures 1 and 2. After some initial trials it was deemed necessary to surround the source with a short glass tube for purposes of initial collimation

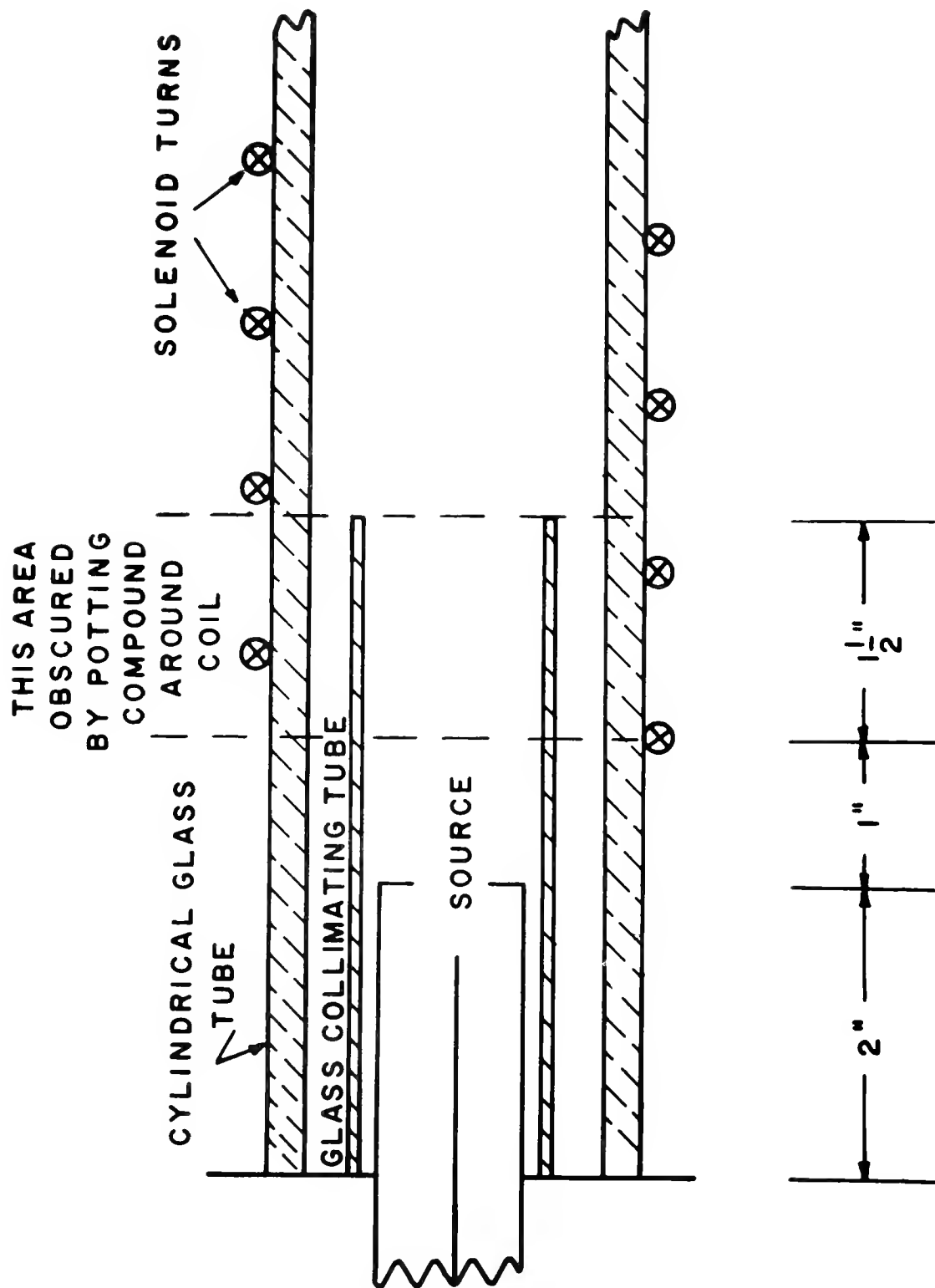


Figure 1

Schematic of Plasma Source with Differential Solenoid





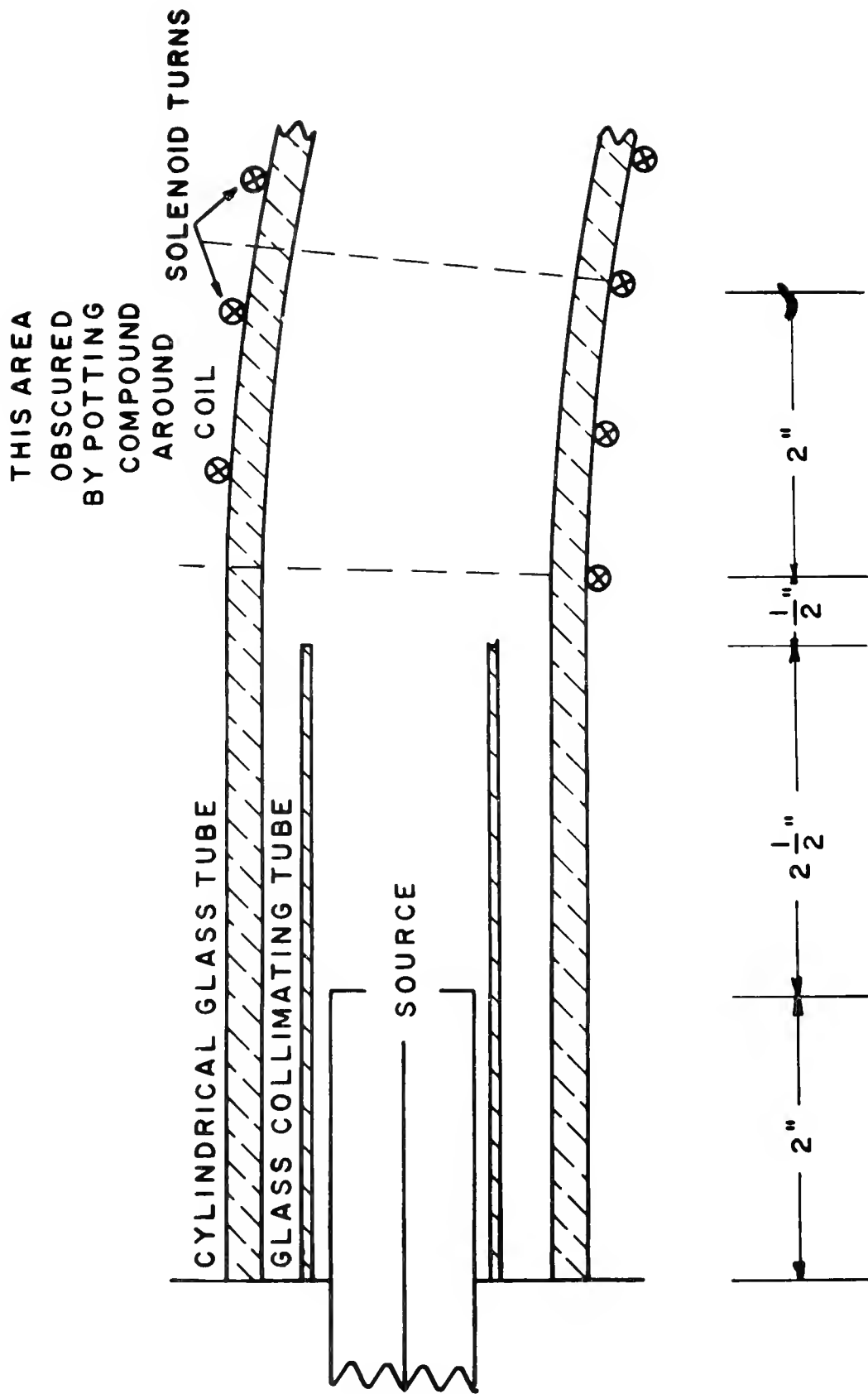


Figure 2

Schematic of Plasma Source with Curved Solenoid



(a technique subsequently reported also by Sinelnikov, et al.<sup>6</sup>); this in no way vitiated the genuineness of the collimating effect provided by the magnetic field, as is amply demonstrated by photographs in which the solenoid was not energized.

It was of some interest to investigate the time pattern of discharge at the source and to compare it to the ringing of the assembly. Examples of these phenomena are shown in Figures 3 and 4. In order to eliminate the effects of noise, the source picture was taken as the output of a photomultiplier at the end of a twenty foot acrylic light pipe which was pointed directly at the mouth of the source. The frequency measured was 1.29 mc. The ringing frequency of the assembly was measured directly across the capacitor; it was 620 kc. (The imperfect wave shape is probably due to poor matching of the voltage attenuation chain.) This is in satisfactory agreement with the assumption that the source fired a sub-burst for a pair of successive half-cycles or full cycles of the assembly (each light peak being not necessarily a plasma sub-burst). A choice between these possibilities is afforded by the data of Section IIIB2.

The brass electrodes of the plasma source were assumed to produce a copper-zinc plasmoid, with all the ions taken at 64 g/g-atom for purposes of computation.

C. Creation of the Axial Magnetic Field: The field was created by one of several solenoid geometries (see E and F, below), within the experimental tube. The pulsed current required was obtained by the discharge of a capacitor bank across

the solenoid using ignitron switching (for mechanical and electrical details, see Appendices I and IV). No special attempt was made to reduce external inductance as high speed was not a requisite.

The bank consisted of eight 105  $\mu\text{F}$  oil and paper capacitors of approximately 0.01  $\mu\text{h}$  each, in parallel and normally charged to 3 kV; total energy was therefore 3780 joules. They were connected by a pair of aluminum sheets separated by Mylar. (Leakage resistance was 600 megohms.) The external inductance (total circuit less bank) was of the order of 8 to 10  $\mu\text{h}$  (depending on solenoid geometry) with about two-thirds contributed by the solenoid.

D. Firing Synchronization: A two-turn search coil was placed around each solenoid. Initial rise in this coil was extremely fast and was taken as "time zero" for purposes of synchronization; return to zero amplitude represented attainment of maximum field in the solenoid. The time-zero signal was used to initiate a time-delay mechanism (see Appendices I and IV) for firing the plasma source, so arranged that the plasmoid reached approximately the center of the solenoid at maximum field. Jitter in this circuit was permissible within wide latitude because the field at maximum changed slowly (first derivative very small) during the plasmoid transit time.

E. The Differential Solenoid: This coil was constructed of 0.12 inch diameter, "half-hard" copper wire, wrapped tightly around a 30-inch-long cylindrical Pyrex pipe, 2.0 inch I.D.,

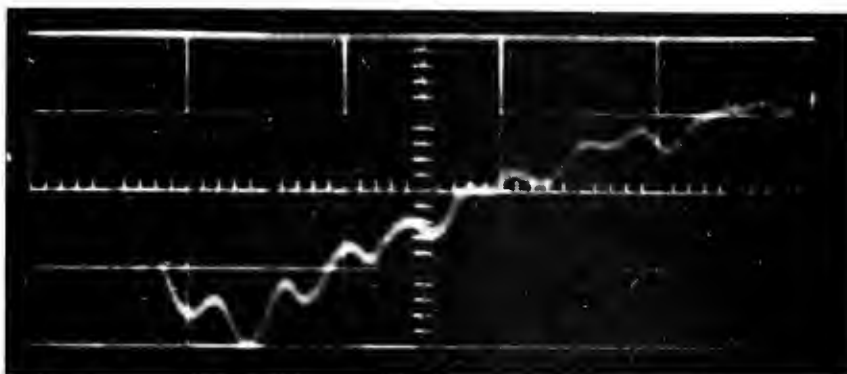


Figure 3  
Light Signal from Plasma  
Source Mouth  
( 1  $\mu$ sec/cm )

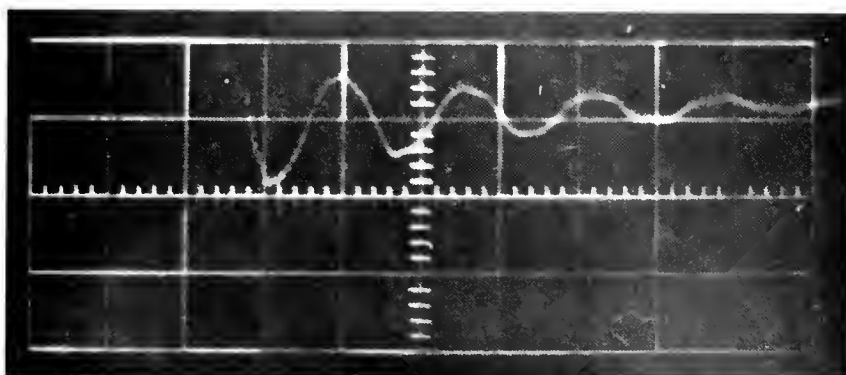


Figure 4  
Ringing of Plasma Source  
and Capacitor Assembly  
( 1  $\mu$ sec/cm )



2.5 inch O.D., producing a current sheath of 1.31 inch radius. The first seven turns were spaced at 1.10 inches per turn, the next nine turns at 0.43 inch, and the remaining eleven turns again at 1.10 inches. The coil was utilized in two different configurations, which will be discussed separately.

1. Normal Differential Solenoid: The bulk of the observations were obtained with the solenoid employed as described above, namely with a central region in which the field intensity was more than double that of the two end regions. The flux line pattern is indicated roughly by Figure 5. This provided the plasmoid with an entrance into and an exit from a magnetic mirror during its transit. The search-coil time for this arrangement is shown in Figure 6 (amplitude is in arbitrary units and is not the same for both pictures). From 6a. one obtains 132  $\mu\text{sec}$  as the time to reach maximum field from time zero. The decay constant,  $\alpha$ , for this damped sinusoidal wave may be obtained from 6b., utilizing the data of the first two extrema:

$$t_1 = 0 \qquad t_2 = 264 \mu\text{sec}$$

$$v_1 = 77 \text{ units} \qquad v_2 = 60 \text{ units}$$

$$\alpha = \frac{10^6}{264-0} \ln \frac{77}{60} = 9.44 \times 10^2 \text{ sec}^{-1}$$

This is also the decay constant for the solenoid; the measured frequency is 1.90 kc.

It is of importance to determine the field strength (i.e., magnitude of magnetic induction) within the solenoid. It was

not convenient to utilize the direct approach of placing a small search coil within the experiment tube. The simplest alternative, therefore, would be to integrate the outside search-coil trace ( $\int V dt$ ), yielding total contained flux, and to divide by the current sheath cross-section. This suffers from two disadvantages. The first is that ascribing to the solenoid the flux seen by the search coil in effect assumes unit coupling between the two coils. Some careful measurements, corroborated by theoretical calculations of mutual inductance, indicated values of the coupling coefficient below 0.3, making this procedure highly uncertain. Second, the distribution of flux is not uniform within the solenoid; although these helices are not bad approximations to true current sheaths, one is not certain, a priori, how close the assumption would be. Thus, even if total flux were obtainable, division by the cross-section would produce only an average field intensity of uncertain validity.

An alternate method would be to calculate the self-inductance which, combined with a knowledge of current, would yield values for the total flux. Calculation of field intensity would still suffer from the second objection noted above. Calculation of inductance for a coil geometry of this sort is difficult. It can be done readily for the three parts of the solenoid on an individual basis, but the mutual end effects are definitely not second order.

In any case, a knowledge of the maximum current would be required. For this solenoid a direct measurement was not made, but the circuit parameters obtained by the search coil, plus



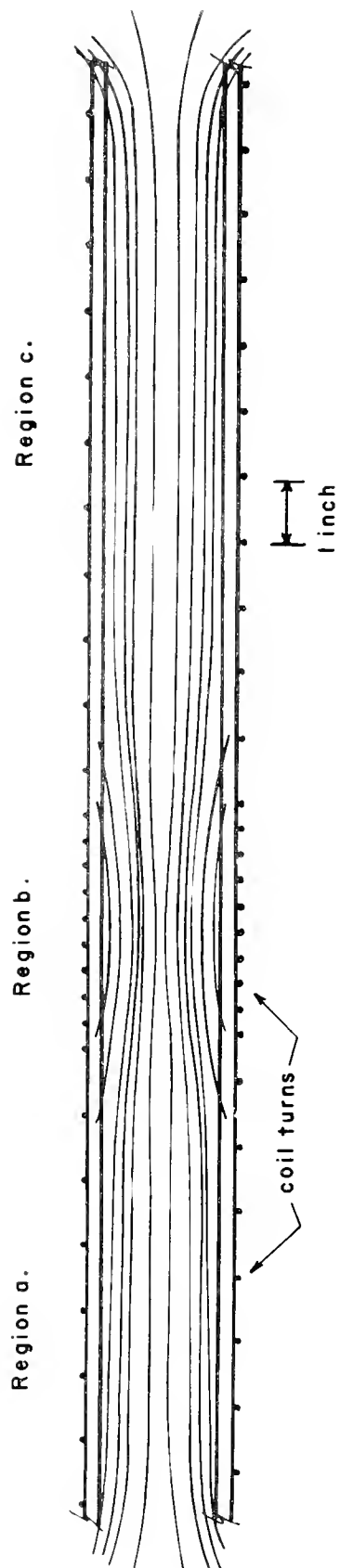
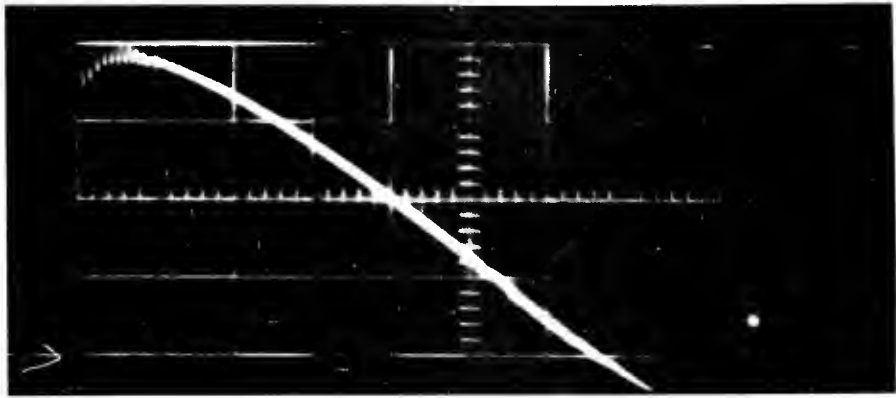
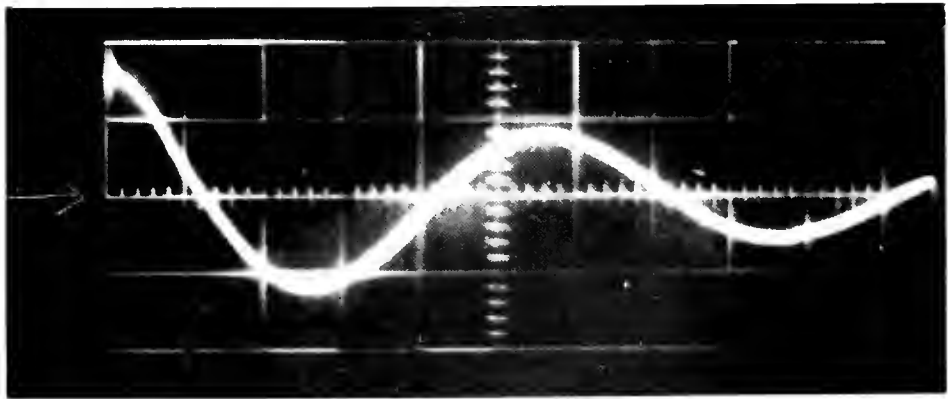


Figure 5  
Flux Line Pattern in Normal Differential Solenoid





6a.  
(20  $\mu\text{sec}/\text{cm}$ )



6b.  
(100  $\mu\text{sec}/\text{cm}$ )

Figure 6  
Two-Turn Search Coil on Normal Differential Solenoid



bank capacitance and initial voltage, are sufficient to yield a reliable value by calculation. The general circuit equation in this case is

$$L \frac{d^2 i}{dt^2} + R \frac{di}{dt} + \frac{i}{C} = 0.$$

Boundary conditions are that  $i = 0$  for  $t = 0$  or infinity. For an under-damped (ringing) circuit, the solution is

$$i = i_{\max} e^{-\alpha t} \sin \omega t,$$

where  $\alpha = \frac{R}{2L}$  and  $\omega = 2\pi f = \left( \frac{1}{LC} - \frac{R^2}{4L^2} \right)^{1/2}$ . (Since  $\alpha$  and  $f$  have been measured, and  $C$  is known, one may calculate  $L$  and  $R$ :

$$(2\pi f)^2 = \frac{1}{LC} - \alpha^2$$

$$L = \frac{1}{C[(2\pi f)^2 + \alpha^2]}$$

$$= \frac{1}{8.4 \times 10^{-4} [(2\pi \cdot 1.9 \times 10^3)^2 + (9.44 \times 10^2)^2]}$$

$$= 8.3 \mu\text{h}$$

and

$$R = 2L\alpha = 2(8.3 \times 10^{-6})(9.44 \times 10^2)$$

$$= 1.57 \times 10^{-2} \text{ ohm.})$$

It may be reasonably assumed that the bank is fully discharged when the current has reached maximum at  $t_1$ . Thus

$$\begin{aligned}
 q_0 &= \int_0^{t_1} i dt = i_{\max} \int_0^{t_1} e^{-\alpha t} \sin \omega t \\
 &= i_{\max} \left[ \frac{e^{-\alpha t} (\alpha \sin \omega t - \omega \cos \omega t)}{\alpha^2 + \omega^2} \right]_{t=0}^{t=t_1} .
 \end{aligned}$$

The value of the function within the brackets, for  $t_1 = 132 \mu\text{sec}$ , is  $8.92 \times 10^{-5}$ . If the initial voltage on the bank is 3 kV, then

$$\begin{aligned}
 i_{\max} &= \frac{C V_0}{8.92 \times 10^{-5}} = \frac{(8.4 \times 10^{-4})(3 \times 10^3)}{8.92 \times 10^{-5}} \\
 &= 28,300 \text{ amp.}
 \end{aligned}$$

This is the undamped maximum current; the actual current,  $i_1$ , at  $t_1$  is given by

$$\begin{aligned}
 i_1 &= i_{\max} e^{-\alpha t_1} \\
 &= 24,900 \text{ amp.}
 \end{aligned}$$

As an alternative to a direct calculation of self-inductance (which, as noted above, would be not only difficult but of limited utility) the following procedure was adopted. The solenoid was approximated by a model consisting of coaxial circular current filaments of equal radii, spaced at intervals which corresponded to the actual turns of the solenoid, twenty-seven filaments in all. Since this resulted in cylindrical symmetry the problem could be reduced to two dimensions by projection on the  $r$ - $z$  plane, with further reduction to the  $r \geq 0$  half. Equations were derived from the Biot-Savart law for the longitudinal and

radial components of the magnetic induction,  $B_z$  and  $B_r$ , for each filament at any point on the  $r$ - $z$  plane (and by symmetry, for any point in space), and then summed over all filaments:

$$B_z = \frac{\mu_0 i}{2\pi\lambda} \left[ \left( \frac{2r_0(r_0 - r)}{\alpha^2} - 1 \right) E + K \right] ,$$

$$B_r = \frac{\mu_0 i}{2\pi\lambda} \left( \frac{z - z_0}{r} \right) \left[ \left( \frac{2rr_0}{\alpha^2} + 1 \right) E - K \right] ,$$

where  $(r, z)$  is the point in question,  $(r_0, z_0)$  the intersection of the filament in the plane, and  $K$  and  $E$  are the complete elliptic integrals of the first and second kind, respectively.

Also one has

$$\lambda^2 = (r + r_0)^2 + (z - z_0)^2 ,$$

$$\alpha^2 = (r - r_0)^2 + (z - z_0)^2 ,$$

and 
$$k^2 = \frac{4rr_0}{\lambda^2}$$

was the modulus of the integrals. The problem was Fortran coded for the IBM 704 computer from which were obtained the values of  $B$  at various significant positions on the half-plane and thus, by symmetry, within the coil (see Appendix VI). The pattern of flux distribution was obtained also, from which Figure 5 was drawn. The problem was run for unit current.

Since the model was based on filaments carrying unit current normal to the solenoid axis, the values of  $B$  obtained should be multiplied by the radial component of the projection of the helical current on the  $r$ - $z$  plane (i.e., the aximuthal current).

This will differ slightly for region b. as compared to a. and c. (Figure 5). Since the distance for a half turn (regions a. and c.) was 0.55 inch while the diameter was 2.62 inches, the azimuthal component of the current is given by

$$i_{az} = i \cos \tan^{-1} \frac{0.55}{2.62}$$

$$= 0.98 i .$$

For a helical current of 24,900 amp, the azimuthal component would be 24,400 amp. In region b. the correction amounts to less than half a percent, and  $i_{az} = i_1 = 24,900$  amp.

This result may now be combined with that of the machine computation to yield field strengths. On the axis the magnitude of magnetic induction was approximately:

central portions of regions a. and c.:	1.1 weber/m <sup>2</sup>
central portion of region b.	: 2.5 weber/m <sup>2</sup> .

Attempts to simplify the picture of the field distribution off the axis suffer difficulties whether one regards the model or the actual helical coil. In the former case moving radially from the axis results in either a decrease or an increase in field intensity depending upon whether z is located between two circular filaments or within one. In the latter case (considering the helix itself), the variation in intensity is dependent upon the angular direction of r for a given z. Thus the model employed here becomes increasingly invalid at substantial distances from the axis. However, values of B, obtained from the machine data, undergo variations of no more than 3 percent at



$r = 0.5$  inch for the central positions of the a. and c. regions and 2 percent for the central portion of the b. region. Most of the plasmoid flow lay well within this radius.

2. Shorted Differential Solenoid: It was of particular interest to obtain some indication of the behavior of the plasmoid as it emerged from and reentered a magnetic mirror (flow through a magnetic bottle). This was accomplished by shorting (and cutting) region b. of Figure 5. The flux line pattern is indicated roughly by Figure 7. Two shorting jumpers are indicated; some photographs were taken with one connected, some with both, as will be noted. The search coil trace for this arrangement is shown in Figure 8 (again, amplitude is in arbitrary units and is not the same for 8a. and 8b.). From 8a. one obtains  $108 \mu\text{sec}$  as the time to reach maximum field. The decay constant may be calculated from 8b., utilizing the data of the second and third extrema (the first being off-scale):

$$t_2 = 200 \mu\text{sec} \qquad t_3 = 416 \mu\text{sec}$$

$$v_2 = 87 \text{ units} \qquad v_3 = 57 \text{ units}$$

$$\alpha = \frac{10^6}{416-200} \ln \frac{87}{57} = 1.21 \times 10^3 \text{ sec}^{-1}.$$

The corresponding frequency is  $2.31 \text{ kc.}$

From these results, the determination of L and R follow (as described in Section E1, above):  $L = 5.6 \mu\text{h};$   
 $R = 1.36 \times 10^{-2} \text{ ohm.}$  Calculation of current, as in E1, yields  $i_{\text{max}} = 34,200 \text{ amp,}$  from which the actual current at maximum field is given by  $i_1 = 30,000 \text{ amp}$  at  $t_1 = 108 \mu\text{sec.}$

This problem also was submitted to computer analysis in a

fashion similar to that of the normal Differential Solenoid. Eight circular filaments represented region a. and twelve, region c., with an appropriate space between (the now inoperative turns of region b.). The pattern of flux distribution is that shown roughly in Figure 7. The values of B obtained were again for unit current and were multiplied by the azimuthal component of  $i_1$ , above, namely  $i_1$  reduced by two percent:  $i_{az} = 29,400$  amp. On the axis the magnitudes of magnetic induction were approximately:

central portions of regions a. and c.:  $1.3 \text{ weber/m}^2$

central portion of region b. :  $0.41 \text{ weber/m}^2$ .

Variations of B off the axis for the central portions of regions a. and c. were less than 3 percent for  $r = 0.5$  inch or less.

The situation in region b. is somewhat more complicated, in part because the plasmoids expanded to the wall of the tube ( $r = 1.0$  inch) and in part because a curving transverse field of some magnitude was created by the jumpers (see Figure 7). On the axis at the center of the b. region the flux density was  $0.41 \text{ weber/m}^2$ , as noted above, decreasing, in the radial direction, by 6.8 percent at  $r = 0.5$  inch and by 25 percent at the wall ( $r = 1.0$  inch). Furthermore, the jumpers created azimuthal fields, normal to the plasmoid flow, of approximately  $0.23 \text{ weber/m}^2$  at  $r = 1.0$  for one jumper and half that value when two jumpers were employed; these values decreased, of course, proceeding inward toward the axis. This is to be compared to  $0.31 \text{ weber/m}^2$  at the inner wall ( $r = 1.0$ ), resulting from the solenoid current.

One additional set of calculations is important. For the

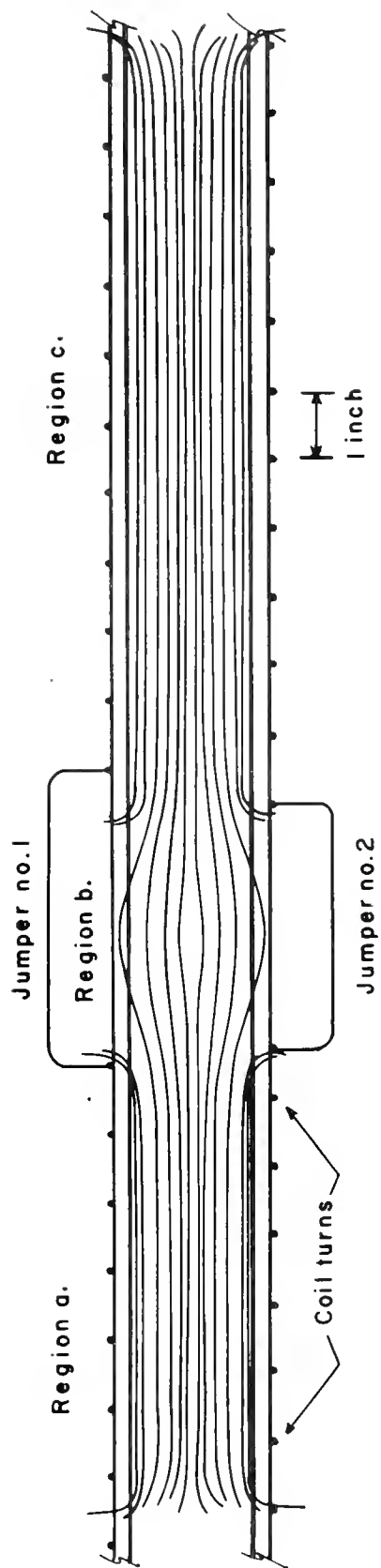
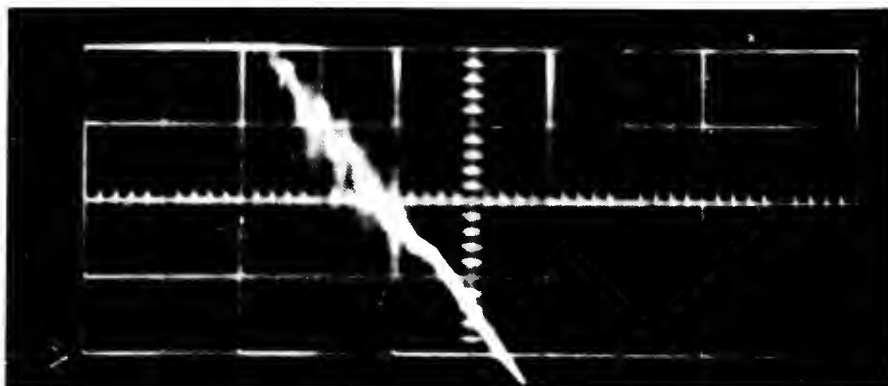
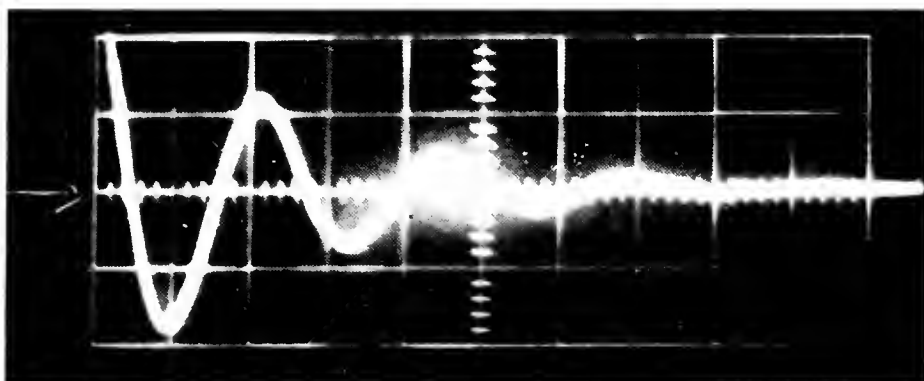


Figure 7  
Flux Line Pattern in Shorted Differential Solenoid





8a.  
(20  $\mu\text{sec}/\text{cm}$ )



8b.  
(200  $\mu\text{sec}/\text{cm}$ )

Figure 8

Two-Turn Search Coil on Shorted Differential Solenoid



Curved Solenoid (to be discussed below) there was no symmetric model available susceptible of straightforward analysis. Thus, it was necessary to obtain a rough measure of field strength, i.e., flux density, through calculation of coil inductance. It is of interest here to ascertain the degree of reliability for such a procedure in a case where independent data on flux density can be obtained; specifically, the last ten turns of region c. in the Differential Solenoid were treated as an independent coil and the inductance was measured directly by a determination of reactance:  $L_c = 1.56 \mu\text{h}$ . Therefore, total flux is given by

$$\begin{aligned}\bar{\Phi} &= \frac{i_{az}L}{N} = \frac{(2.94 \times 10^4)(1.56 \times 10^{-6})}{10} \\ &= 4.59 \times 10^{-3} \text{ weber.}\end{aligned}$$

Cross-section for  $r = 1.31$  inch is  $3.50 \times 10^{-3} \text{ m}^2$ . Therefore,  $B_{av} = 4.59 \times 10^{-3} / 3.5 \times 10^{-3} = 1.31 \text{ weber/m}^2$ . This is to be compared to a machine calculation of axial field strength for an eleven circular filament model, which yielded  $B = 1.30 \text{ weber/m}^2$ . The correspondence is quite fortuitous; there are a number of errors inherent to this procedure but fortunately many of them cancel, suggesting that it is feasible.

F. The Curved Solenoid: The other major geometry investigated was a solenoid which created a curved field. The Pyrex experiment tube was about 45 inches long, with 2 inch I.D. and 2.3 inch O.D. Thirty-one turns of 0.12 inch diameter, "half-

hard" copper were wrapped tightly around at a mean arc spacing of 1.05 inches per turn, producing a current sheath of 1.20 inch radius. This solenoid approximated a  $60^\circ$  arc; radius of curvature for this geometry (as well as the length of the chord) was 31 inches. The flux pattern is indicated roughly in Figure 9. The field is not distributed with axial symmetry, of course, being somewhat more concentrated toward the center of curvature; however, the effect is not as exaggerated as in the figure. For a rough estimation of field distribution in geometries of this sort one may assume that the product  $rB$  is a constant, where  $r$  is the distance from the center of curvature to some point within the coil on the curvature plane. From this one may readily deduce that the logarithmic gradient of  $B$  (i.e.,  $|\nabla B|/B$ ) is roughly equal to the reciprocal of  $r$  at that point. Thus, variation in flux density due to curvature should amount to approximately 6 percent within the tube.

The search-coil trace for this arrangement is shown in Figure 10 (again, amplitude is in arbitrary units and is not the same for 10a. and 10b.). Figure 10a. shows the time to reach maximum field as 120  $\mu\text{sec}$ . The decay constant is again calculated, from Figure 10b, using the first and second extrema:

$$t_1 = 0$$

$$t_2 = 240 \mu\text{sec}$$

$$v_1 = 80 \text{ units}$$

$$v_2 = 57 \text{ units}$$

$$\alpha = \frac{10^6}{240-0} \ln \frac{80}{57} = 1.41 \times 10^3 \text{ sec}^{-1}.$$

The corresponding frequency is 2.09 kc. Values of  $L$ ,  $R$ , and



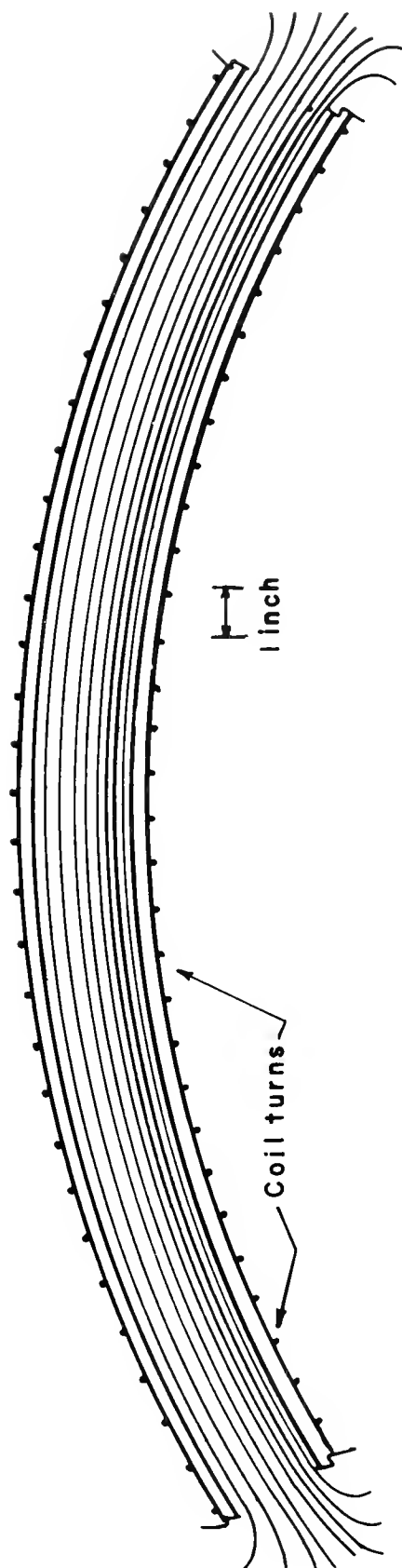
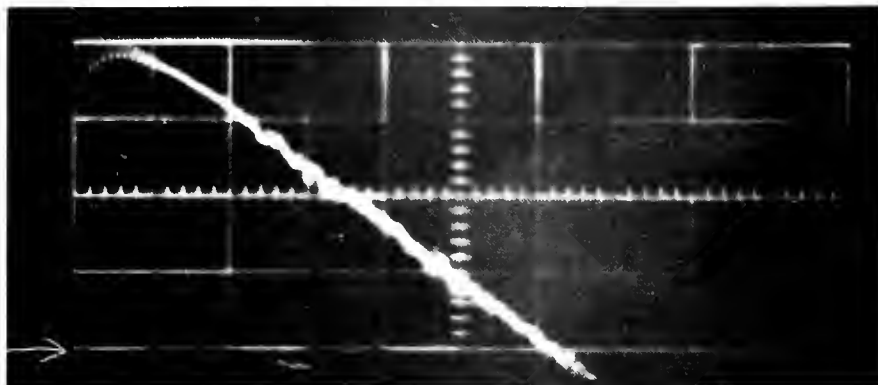
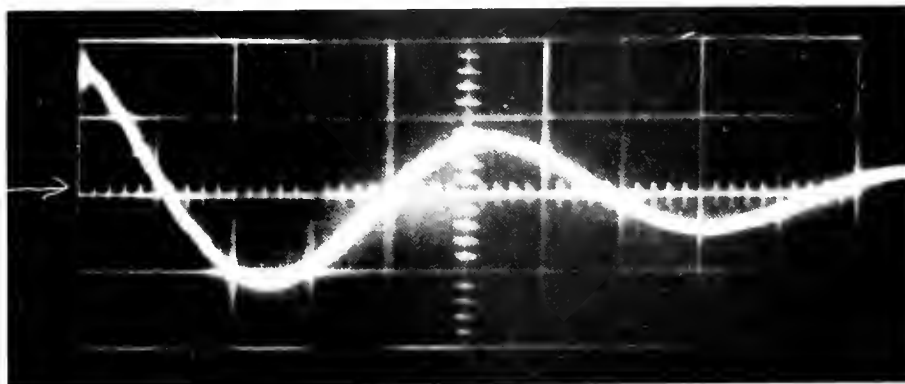


Figure 9  
Flux Line Pattern in Curved Solenoid





10a.  
(20  $\mu$ sec/cm)



10b.  
(100  $\mu$ sec/cm)

Figure 10  
Two-Turn Search Coil on Curved Solenoid



$i_{\max}$  are again calculated as in Section E1, above:  $L = 6.8 \mu\text{h}$ ;  $R = 1.9 \times 10^{-2} \text{ ohm}$ ;  $i_{\max} = 30,800 \text{ amp}$ . The actual current at maximum field was  $i_1 = 26,000 \text{ amp}$  at  $t_1 = 120 \mu\text{sec}$ . Azimuthal current is again about two percent less, or  $i_{az} = 25,400 \text{ amp}$ . It is of interest to note that in this instance an independent measure of current was obtained to determine the validity of these mathematical procedures. A strip of manganin metal was placed in series with this solenoid and the potential drop recorded by an oscilloscope during bank discharge. At 3 kV, the maximum of the trace was 29.0 V. The resistance of the manganin strip was measured independently, yielding  $1.11 \times 10^{-3} \text{ ohm}$ . The current at maximum discharge was therefore 26,100 amp, which corresponds quite closely to  $i_1$  above.

As has been discussed in Section E2, above, there is no model for this solenoid which possesses sufficient symmetry to permit straightforward determination of flux distribution even by machine computation, at least with the degree of relative simplicity permitted by the Differential Solenoid. It was therefore necessary to proceed by the approximation method already discussed, and shown to be reasonably valid, employing measured inductance. From an inductive reactance measurement on this coil,  $L = 4.87 \mu\text{h}$  for 31 turns. Therefore, total flux is given by

$$\begin{aligned}\Phi &= \frac{i_{az} L}{N} = \frac{(2.54 \times 10^4)(4.87 \times 10^{-6})}{31} \\ &= 3.99 \times 10^{-3} \text{ weber.}\end{aligned}$$

Cross-section for  $r = 1.20 \text{ inch}$  is  $2.92 \times 10^{-3} \text{ m}^2$ . Therefore,  $B_{av} = 3.99 \times 10^{-3} / 2.92 \times 10^{-3} = 1.37$  or approximately  $1.4 \text{ weber/m}^2$ .

#### G. Center-of-Mass and Expansion Velocity Measurements:

Two parameters of the plasmoid which could be obtained in a fairly straightforward fashion were velocity of the plasmoid center-of-mass and the rate of expansion of the plasmoid during flight. Both were obtained as the result of the same series of measurements, namely time-of-flight studies with photomultipliers, using the normal Differential Solenoid.

Preliminary observations suggested considerable variability in timing with respect to various attempted methods of oscilloscope triggering ("jitter"). To eliminate the trigger as a time marker, three photomultipliers were employed, one focused at about the third turn of region a., 8 cm from the mouth of the source, the second at the boundary of regions a. and b., and the third at the boundary of regions b. and c. The resulting distances of plasmoid traverse were 11.5 cm and 10.5 cm for regions a. and b., respectively. Thus, two different sets of results were obtained simultaneously for each plasmoid burst. The photomultiplier outputs were run into three oscilloscopes of the same model and make, the sweep generators of which had been mutually calibrated, and suitable triggering was employed to minimize trace-time error (see Appendix V for further details).

Calculation of center-of-mass velocity depended upon the assumption that the center of mass would coincide at all times with location of maximum recombination light intensity. Expansion velocity, on which maximum temperature was based, was deduced from the rate of longitudinal expansion of the photomultiplier trace between each of the two pairs of locations. Usually this was

calculated from the increase in half-width of a light peak, measured at half-amplitude (to be discussed further with the data in Section III). While this method of ion-temperature determination is not trustworthy, compared to presently available methods, it gains considerably in simplicity, particularly where only an upper bound is required.

### III. Results and Discussion

A. General: A large portion of the reported data consists of time-integrated photographs of plasmoid behavior when they are injected in the normal Differential Solenoid. The pattern of the flow is compared to that of the field configuration. Utilizing this same arrangement, time-of-flight data were obtained, from which variations in velocity and temperature are deduced. A method of shock-heating the original spark channel is suggested. On the basis of these results, and some additional measurements, a value for density is obtained. Assumptions of electron temperature are suggested, from which a degree of ionization is calculated. From this, Larmor radius and drift velocity follow. A total reflection coefficient for the plasmoid is calculated, viewing the constriction of field in the b. region as a magnetic mirror. In addition, an estimation is made of the magnitude of the plasmoid self-field, as compared to the superimposed  $B_z$  field.

Time-integrated photographs are then shown of the shorted Differential Solenoid under certain varied conditions. Finally, photographs are shown of plasmoid behavior in the Curved Solenoid with variations of both plasmoid and field energy, and the effects are calculated of an internal polarization field due to charge separation.

B. Plasmoid Flow in the Normal Differential Solenoid: This section is divided into photographic results, photomultiplier measurements, and derived results. The axial values of magnetic induction are given in each case, for regions a. and c. and for region b. These values were varied somewhat for the photographic results (by changing initial voltage) to accentuate certain phenomena. The plasmoid source was fired at 12 kV, producing an



energy per burst of 40 joules. Synchronization was arranged to place the burst approximately 10 cm within region a. at maximum field.

1. Photographic Results: Pictures were taken of individual bursts, with shutter open and aperture adjusted to minimize peripheral light (slower fragments of the plasmoid that had expanded to the walls) and accentuate the flow path of the central portion of the burst. The photographs shown here are representative of an extensive amount of reproducible data.

An example of the flow pattern of the plasmoid is given in Figure 11, in which are included a camera field-of-view picture of the solenoid and a picture of plasmoid discharge without magnetic field.

In this type of photography the appearance of the plasmoid flow in the picture (for any given set of experimental conditions) is strongly influenced by camera aperture. A series of pictures was taken with gradually decreasing aperture while holding all other conditions constant. These are shown in Figure 12. Not only the brightness but the curvature of the flow outline is altered on diminishing aperture (Figures 12g. and 12h.) The central, denser portions of the plasmoid pass into the mirror between regions a. and b. with little constriction. The fact that the photographs are time integrated raises the possibility (further suggested by time-of-flight studies, below) that the leading edge or first sub-burst of the plasmoid is considerably less affected by the mirror than the remainder, and it may be the passage of this portion which is being recorded in the smaller

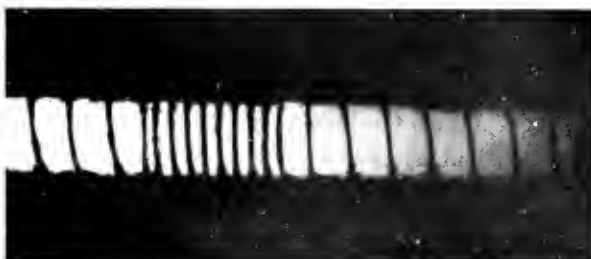
aperture pictures.

A datum which will be of later interest may also be obtained from this series of figures, namely an estimate of the plasma drift across a uniform field. Figure 12f. is most convenient for this purpose since it appears to show largely the flow of the leading edge or high density sub-burst (as described above). There are six turns visible in region c. of this figure. If one examines the flow between the second and sixth turns (where the field is reasonably uniform) one finds an increase in plasmoid diameter of approximately two percent, or a transverse drift velocity of about one percent of the axial velocity.

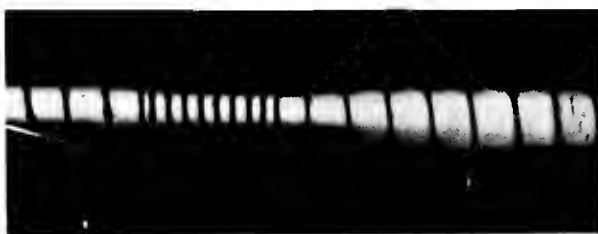
The next point of interest concerns variations in flow pattern when the field is changed. Figure 13 shows an example of the effect of doubling the field. At the lower field strength there is a constriction in region b.; while doubling the field produces a smaller beam in region a., it does not appear to constrict further the dense portion of the plasmoid flow in region b. It does, however, reduce the hazy light (presumably the cooler, trailing portions of the plasmoid). Apparently there is a limit to the degree of constriction obtainable under these particular conditions. This phenomenon was examined with close-up photography, as is shown in Figure 14. Here (in 14d.) it is seen clearly that there is a dense portion of the plasmoid which appears to experience no further constriction when entering region b., if the field is already beyond some (unspecified) magnitude.



11a.  
Solenoid



11b.  
Plasma: 40 joules



11c.  
Plasma: 40 joules  
Regions a. and c.:  
0.73 weber/m<sup>2</sup>  
Region b.: 1.65 webers/m<sup>2</sup>

Figure 11  
Plasmoid Flow in the Normal Differential Solenoid.I.





12a.  
Solenoid



12b.  
No field  
Aperture: f 16



12c.  
Aperture: f 16



12d.  
Aperture: f 16 - 22

Figure 12

Plasmoid Flow in the Normal Differential Solenoid.

II. Study of Camera Interpretation

Plasma: 40 joules

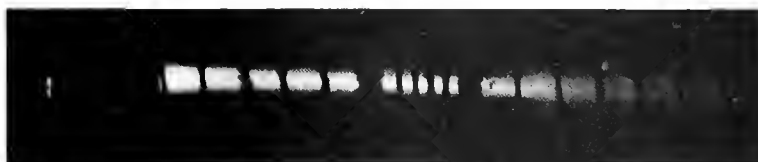
Regions a. and c.:  $0.55 \text{ weber/m}^2$

Region b.:  $1.25 \text{ webers/m}^2$

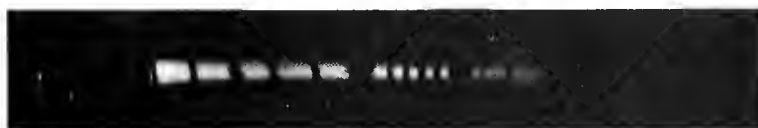




12e.  
Aperture: f 22



12f.  
Aperture: f 22 - 32



12g.  
Aperture: f 32



12h.  
Aperture: f 32 - 45

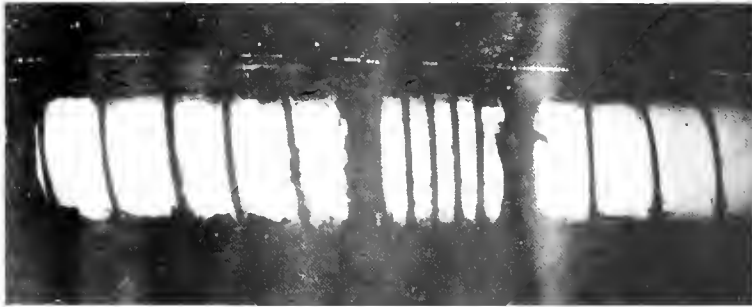
Figure 12 continued







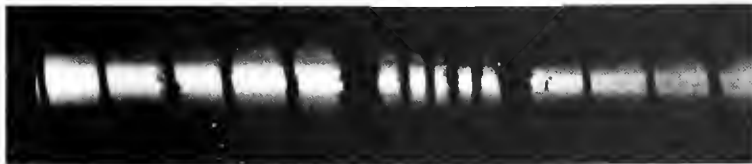
13a.  
Solenoid



13b.  
Plasma: 40 joules  
No field



13c.  
Plasma: 40 joules  
Regions a. and c.:  
0.55 weber/m<sup>2</sup>  
Region b.: 1.25 webers/m<sup>2</sup>  
Aperture: f 16 - 22



13d.  
Plasma: 40 joules  
Regions a. and c.:  
1.1 webers/m<sup>2</sup>  
Region b.: 2.5 webers/m<sup>2</sup>  
Aperture: f 22

Figure 13

Plasmoid Flow in the Normal Differential Solenoid.  
III. Effect of Field Variation





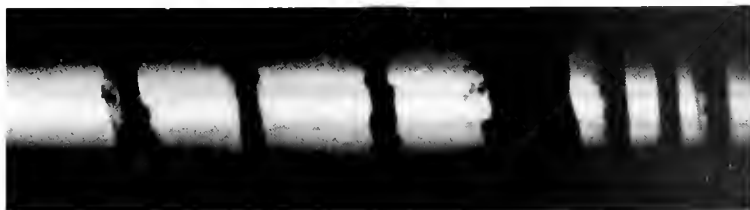
14a.  
Solenoid



14b.  
Plasma: 40 joules  
No field



14c.  
Plasma: 40 joules  
Regions a. and c.:  
0.55 weber/m<sup>2</sup>  
Region b.: 1.25 webers/m<sup>2</sup>  
Aperture: f 16 - 22



14d.  
Plasma: 40 joules  
Regions a. and c.:  
1.1 webers/m<sup>2</sup>  
Region b.: 2.5 webers/m<sup>2</sup>  
Aperture: f 22

Figure 14

Plasmoid Flow in the Normal Differential Solenoid.  
IV. Effect of Field Variation in Close-up



Another feature of Figure 14d. is the striation of the plasmoid flow. A filament of plasma across the top of the tube is diverted inward upon entering the mirror. This appears more clearly in Figure 15. It is not easy to decide whether this filament is part of the initial, high density sub-burst (which is seen more clearly in Figure 14d.) or is part of the trailing material which makes up the general haze surrounding the main beam, although the latter is more likely.

The data from machine computation described in Section II E1, above, provide an opportunity to examine some details of the plasmoid flow in comparison to the known behavior of flux lines (assuming accuracy of the model employed). Figure 14c. provides a reasonably clear picture of plasmoid constriction upon entering the mirror region; Figure 15 is particularly interesting for the presence of the single filament of plasma. These two flow patterns have been transposed to Figure 16, together with points (marked x) tracing three flux lines which lie in the immediate vicinity of the pattern outlines. A flux line (actually, the trace of a stream function) is to be interpreted as the generator of a surface of axial revolution upon which there is no normal component of  $\vec{B}$  (i.e., no flux crosses this surface). Radial coordinates are relative to the center of the solenoid and axial coordinates are relative to the position of the first turn. The locations of turns (per the model) are shown. Magnitudes of  $B$  are radially constant to better than one percent within the volume occupied by the plasmoid. Actual values of flux and magnetic induction are not given on the diagram as it is composed

of data taken at two different values of solenoid current.

The correspondence between the outer flux line and the plasma filament is good, that between the center and inner lines and the outlines of the central flow of the plasmoid is not, particularly to the left where there is a greater uncertainty in the location of the plasmoid flow boundary. Some of the discrepancy may be laid to difficulties of transposition from photograph to figure and some to the small scale errors due to employing the circular current filament model. But primarily the problem involves a decision as to the location of the boundary in region a. by which we might define the outline of the central, dense portion of the flow. One may estimate its radius to be about 0.2 inch or more in region a. and about 0.12 inch in region b.

2. Photomultiplier Measurements: The techniques employed were described in Section IIG. All data reported here were of a single 40 joule plasmoid fired into the tube without field or with a field of  $1.1 \text{ webers/m}^2$  on the axis of the a. and c. regions and  $2.5 \text{ webers/m}^2$  on the axis at the center of the b. region. A representative series of three oscilloscope traces is shown in Figure 17 for a plasmoid transit without field (signals are negative-going and of arbitrary amplitude). As previously stated, these represent points located toward the beginning of region a., at the a.-b. transition and at the b.-c. transition, with separations of 11.5 cm and 10.5 cm, respectively.

Figure 17a. suggests the presence of a double peak in the plasmoid but as it progresses down the tube this distinction



Figure 15

Plasmoid Flow in the Normal Differential Solenoid.

V. Diverting of Plasma Filament

Plasma: 40 joules  
Regions a. and c.:  $1.1 \text{ webers/m}^2$   
Region b.:  $2.5 \text{ webers/m}^2$   
Aperture: f 16





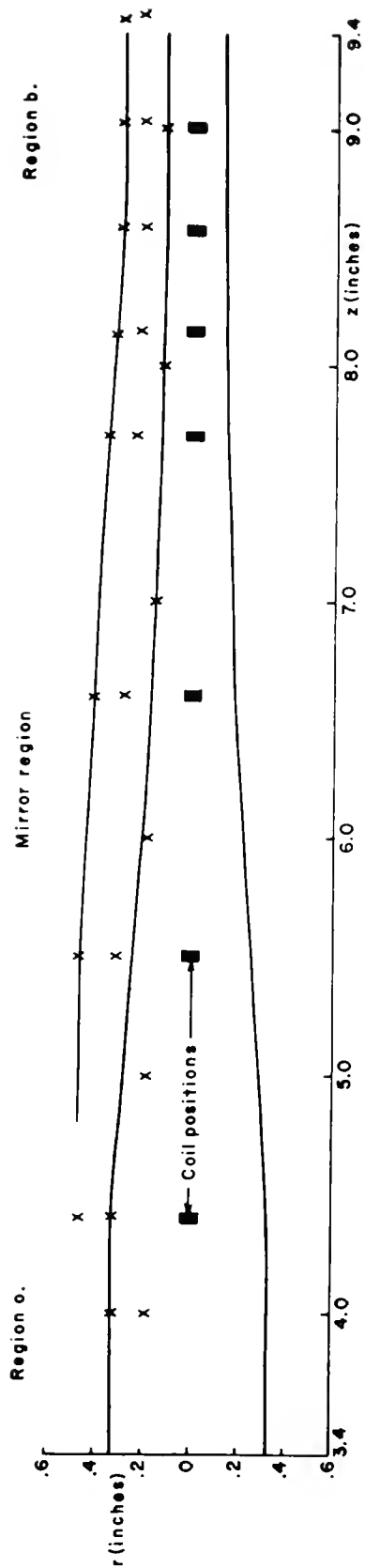
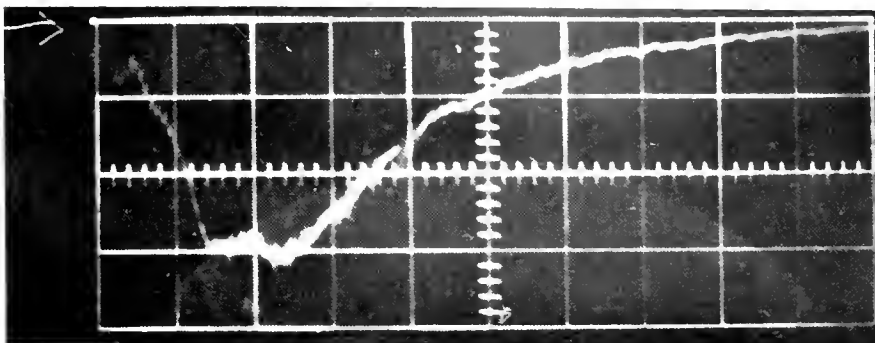
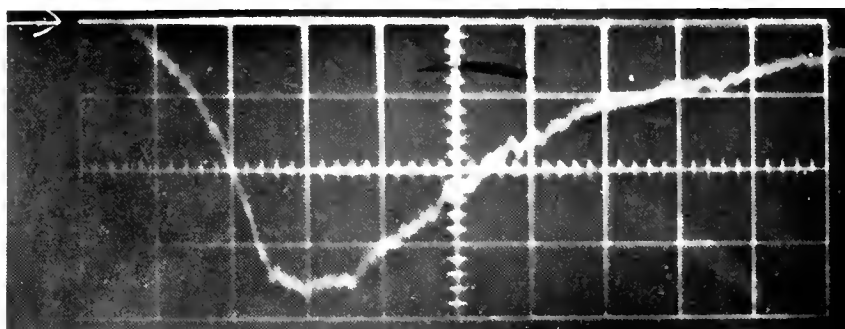


Figure 16  
Plasmoid Flow vs. Flux Line Behavior at a Magnetic Mirror

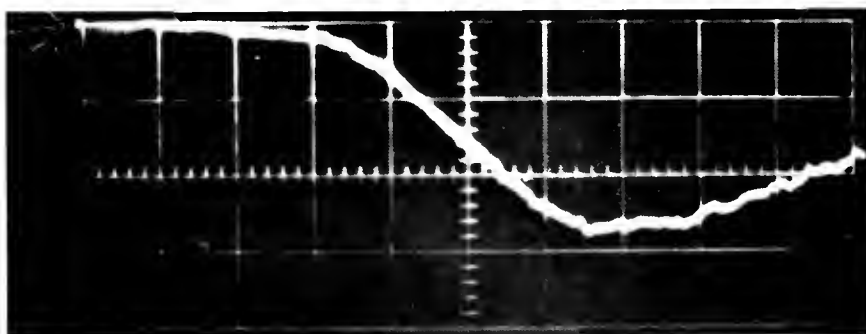




17a.  
Position: 8 cm  
(2  $\mu$ sec/cm)



17b.  
Position: 19.5 cm  
(2  $\mu$ sec/cm)



17c.  
Position: 30 cm  
(2  $\mu$ sec/cm)

Figure 17

Photomultiplier Traces of Plasmoid Transit without Field



vanishes and the plasmoid becomes continuous. This was found to be true in all cases when a guiding field was absent. Taking the center of each peak (or the twin peak in the case of 17a.), the time of transit between positions was determined for a number of runs and averaged. The resulting velocities of the center of mass of the plasmoid in regions a. and b. were then obtained by dividing 11.5 cm and 10.5 cm by the respective transit times. An upper bound to the thermal velocity was obtained by choosing the point on each curve which was at half maximum following the peak and similarly determining its velocity. These velocities subtracted from those of the center of mass gave a measure of the speed with which the plasmoid was expanding. For example, the center-of-mass velocities in regions a. and b. were  $v_a = 5.5 \text{ cm}/\mu\text{sec}$ ,  $v_b = 1.30 \text{ cm}/\mu\text{sec}$ . The velocities of the half-maxima following the peak were 3.8 and 0.93 cm/ $\mu\text{sec}$ , respectively. Therefore, the expansion velocities in regions a. and b. were at most  $v_{ta} = 1.7 \text{ cm}/\mu\text{sec}$  and  $v_{tb} = 0.37 \text{ cm}/\mu\text{sec}$ .

A representative set of data for time-of-flight studies in a magnetic field is shown in Figure 18 (again signals are negative-going and of arbitrary amplitude). Photomultiplier positions are the same as before. The double peak is now not only distinct in the first position (Figure 18a.) but it appears to be maintained to some extent during the transit of the plasmoid along the tube (4 and 8  $\mu\text{sec}$  in Figure 18b. and 6.5 and 15.5  $\mu\text{sec}$  in Figure 18c.). This suggested that the sub-bursts ought to be analysed separately, which was done. They will be identified as the leading (L) and trailing (T) peaks.

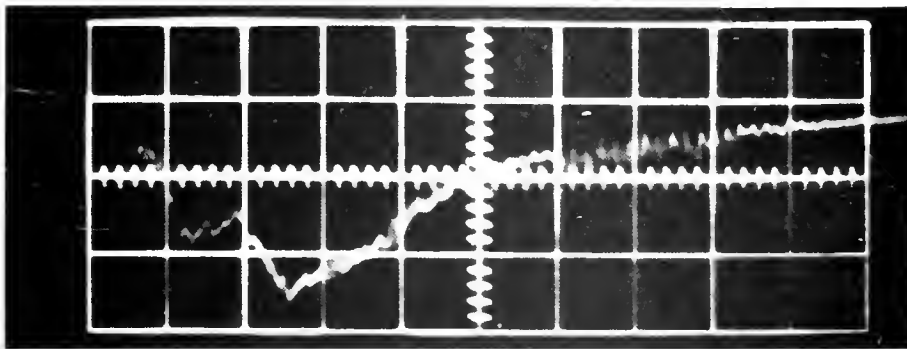
Center-of-mass velocities were calculated from assembled data for both peaks L and T in regions a. and b. Expansion velocity determinations for peak T were readily performed as in the case of no field, above, utilizing the variation in velocity of the half-maximum which followed peak T. In the case of peak L, the shape of the curve did not lend itself to this procedure (e.g., using the half-maximum which preceded L) and there were problems connected with relative rise-times of the three photomultipliers. Therefore, a reasonably reproducible technique was employed for estimating the change in the half-width of peak L; this result was attributed to expansion velocity associated with temperature.

Table 1 summarizes the results of the photomultiplier study, where  $v_a$ ,  $v_b$  designate center-of-mass velocity in regions a. and b., and  $v_{ta}$ ,  $v_{tb}$  designate expansion velocity:

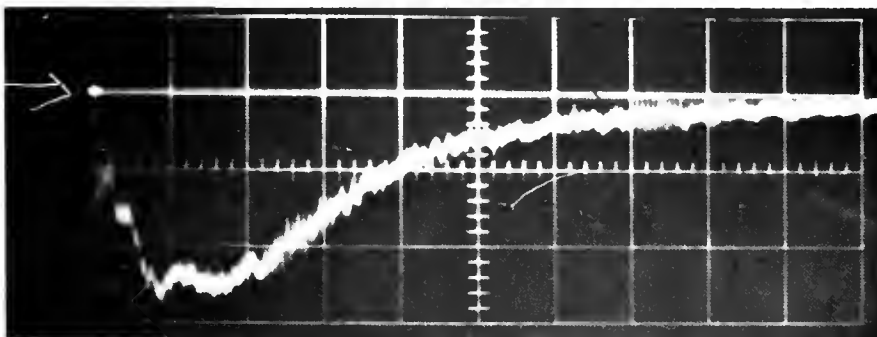
Table 1

	<u>No Field</u>	<u>Field</u>	
		(L)	(T)
$v_a$	5.5	5.5	3.3 cm/ $\mu$ sec
$v_b$	1.3	5.3	1.65 cm/ $\mu$ sec
$v_{ta}$	1.7	1.8	1.9 cm/ $\mu$ sec
$v_{tb}$	0.37	1.9	0.55 cm/ $\mu$ sec
$(v_a/v_b)^2$	18	1	4
$(v_{ta}/v_{tb})^2$	21	1	12

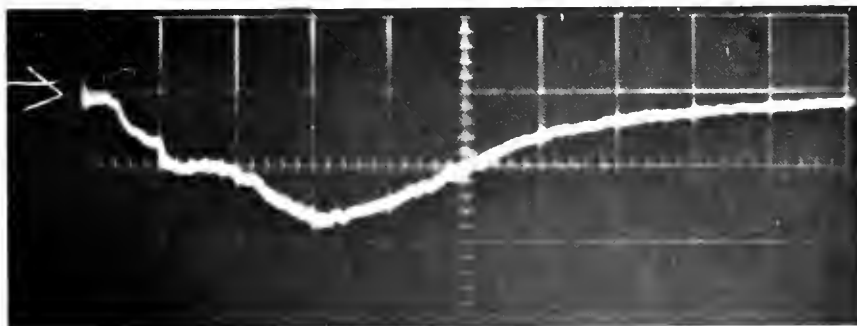
The fifth and sixth lines represent the decrease in energy for center-of-mass velocity and expansion velocity, respectively.



18a.  
Position: 8 cm  
(2  $\mu$ sec/cm)



18b.  
Position: 19.5 cm  
(5  $\mu$ sec/cm)



18c.  
Position: 30 cm  
(5  $\mu$ sec/cm)

Figure 18

Photomultiplier Traces of Plasmoid Transit with Field





The following observations may be made. First, without field the plasmoid behaves predominantly as a single puff of plasma which gradually loses kinetic energy of both center-of-mass and expansion motion at about the same rate. One may presume that residual gas within the tube (density of  $1.6 \times 10^{11}$  molecules/cc at pressure of  $5 \times 10^{-6}$  mm Hg) barely contributes to this deceleration (mean free path in  $N_2$  is about two meters). However, the limitation of the tube wall has become a major factor by the time the plasmoid has reached region b. When a guiding field is provided, however, the two sub-bursts, which appear to be formed initially, maintain their identity. The behavior of L in region a. with field is identical (within experimental error) with that of the entire plasmoid without field (i.e., both center-of-mass and expansion velocities are the same). However, with field, L is able to maintain the magnitude of both velocities in region b. Conversely, T not only starts (in region a.) with both velocities lower but has lost considerable energy by the time it has reached region b.

Third, it is interesting to compare energy loss without and with field (the T peak). As noted above, the former case shows equal energy loss for both center-of-mass and expansion velocities, while in the latter case energy loss associated with the center of mass is the smaller of the two, and both are less than is the case without field. For one, a confining field will eliminate energy losses to the walls. In addition, higher density shortens the mean free path for all two-body processes, possibly increasing the rate of recombination, and radiative cooling.

The expansion velocity of 1.9 cm/ $\mu$ sec for atomic weight 64 may be associated with an ion "temperature" of 120 eV by  $w_1 = Mv^2/2 = kT$ . There are several reasons for which the true kinetic temperature may be less. For one, the axial expansion of the plasmoid from its center of mass may be due to a spatial variation in initial axial velocity among the ions which received the initial impulse. Second, the distribution of relative velocities may be strongly anisotropic at  $t = 0$ , and this spread in axial velocities may not have become randomized. Third, while it is convenient to assume that the plasmoid is macroscopically neutral, this need not be exactly true. Small deviations from neutrality would also contribute to an increase in expansion velocity, not properly equatable to temperature. Therefore  $w_1 = 120$  eV must be considered an upper bound. This is quite adequate to show that the flow is supersonic. It is of interest to note, however, that the plasmoid expands rapidly to the tube walls when no confining field is applied; this may be seen most clearly in Figure 22b (vide infra) which must be compared to Figure 2 for appropriate dimensions. Here the plasmoid has a distance of about one-half inch to expand to the tube wall, and this is accomplished in an axial distance which is clearly smaller than two inches, suggesting that even radial expansion velocity is greater than one-quarter of the axial, center-of-mass velocity. Lack of neutrality would, of course, be an operative factor in this case, also.

The formation of sub-bursts, L and T, probably is due to the ringing of the plasma source capacitor. If one ascribes the velocities of 5.5 and 3.3 cm/ $\mu$ sec to L and T, respectively, at

the position of the first photomultiplier, 8 cm from the source mouth, then L required 1.5  $\mu$ sec, and T, 2.4  $\mu$ sec, to travel that distance. Since Figure 18a. shows L as having arrived 2.6  $\mu$ sec after (some arbitrary) time zero, and T at 5.2  $\mu$ sec, then L started at the source mouth at 1.1  $\mu$ sec and T, at 2.8  $\mu$ sec. The two peaks were therefore separated a time 1.7  $\mu$ sec initially, a frequency of 610 kc, corresponding closely to the measured 620 kc of the capacitor (Section IIB).

3. Derived Results: An indication of the quantity of material released on a single burst was obtained by firing once with the vacuum manifold closed, and measuring the pressure. This was more likely to be a measure of entrapped electrode gas than of metal ions but it provided a rough figure for test purposes; there was no doubt that it correctly reflected electrode (plasma source) decomposition since pressures obtained were proportional to the square of the plasma source voltage.

A reading of  $5.8 \times 10^{-4}$  mm Hg was obtained for a system volume of 13.8 liters. The plasmoid was formed with a diameter of about 1.5 cm; it passed the first photomultiplier with a mean speed of 4.4 cm/ $\mu$ sec and lasted for about 12  $\mu$ sec (see Figure 18a.). Total length was therefore about 53 cm and volume, 94 cc. Ion pressure within this plasmoid would thus have been  $(5.8 \times 10^{-4})(13800/94) = 8.5 \times 10^{-2}$  mm Hg at room temperature, and the corresponding mean number density, n, utilizing perfect gas law) was about  $2.7 \times 10^{15}$  ions/cc; in the 94 cc there were  $2.5 \times 10^{17}$  ions.

The method employed is questionable and the result is high.

A significant portion of the plasmoid may have contained trapped neutral material which was carried along. The result should be regarded as an upper bound.

One may test its validity to some extent as follows although the above objection would not necessarily be obviated. Assume that the center-of-mass velocity imparted to the leading sub-burst was derived entirely from the magnetic energy resulting from the discharge. The ion density at the source, of this sub-burst, will not be the same as  $n$ , above, but higher. Assume that not more than  $10^{17}$  ions are contained in this sub-burst. Cross-section will be that of the center electrode (location of highest current density) where  $d = 0.33$  cm. A sub-burst lasts about  $1.7 \mu\text{sec}$  (vide supra); at  $v = 5.5 \text{ cm}/\mu\text{sec}$  this amounts to  $9.5$  cm of length. Volume is therefore  $0.8 \text{ cc}$  and density is  $1.2 \times 10^{17}$  ions/cc, at the source. The kinetic energy density may be written as  $\rho v^2/2$  where  $\rho$  is the mass density and  $v$  is the resulting velocity. This may be equated to the magnetic energy density  $\mu_0 H^2/2$ . The value of  $H$  is not known directly for the plasmoid discharge, but one may substitute  $I/l$  where  $l$  is some characteristic distance. Since the center electrode diameter is about  $0.33$  cm,  $l$  will be taken as  $0.33\pi \times 10^{-2}$  m. A rough measure of  $I$  (at maximum discharge) is given by  $(3/2)(q/\Delta t)$  where  $q$  is the initial charge on the capacitor and  $\Delta t$  is the time for a quarter wave (in this case,  $4.1 \times 10^{-7}$  sec). At  $12 \text{ kV}$  and  $0.55 \mu\text{F}$ ,  $I = 2.4 \times 10^4$  amp. For  $n = 1.2 \times 10^{17}$  ions/cc,  $\rho = 1.3 \times 10^{-2} \text{ kg/m}^3$  (taking a mean atomic weight of  $64$ ). Therefore, one obtains

$$\begin{aligned}
v &= \left( \frac{\mu_0}{\rho} \right)^{1/2} \left( \frac{I}{l} \right) \\
&= \left( \frac{4\pi \times 10^{-7}}{1.3 \times 10^{-2}} \right)^{1/2} \left( \frac{2.4 \times 10^4}{0.33\pi \times 10^{-2}} \right) \\
&= 2.1 \times 10^4 \text{ m/sec} \\
&= 2.1 \text{ cm}/\mu\text{sec},
\end{aligned}$$

which is to be compared to the measured velocity of 5.5 cm/ $\mu$ sec; the 2.5-fold discrepancy reflects the uncertainty in the computation.

These numbers may be used for another purpose, to estimate an upper bound for the self-field created by any possible plasmoid currents. The simplest assumption would be that the initial discharge current and consequent field is larger than any subsequently developed in the plasmoid. The induction created in this case is then given directly by  $B = \mu_0 I/l = 3 \text{ weber/m}^2$ . However, the plasmoid cross-section increases rapidly by a factor of  $(1.5/0.33)^2 = 21$ , so that the plasmoid's effective field would be well below that of the solenoid.

It is of interest now to consider the nature of the plasmoid discharge (with particular attention to ion and electron temperatures and degree of ionization) during the time that current is flowing between the electrodes and shortly thereafter, a period of the order of 4  $\mu$ sec. Continuous arcs have been studied extensively as part of the general subject of gas discharge, with Edels<sup>10</sup> making a particular subject of the study

of the temperature of individual species within the discharge. The problem here is a rather different one, however, in that times of interest are extremely short and the discharge is formed along a surface in initially high vacuum conditions. Transient vacuum sparks have been described by Boyle, et al.<sup>11</sup> For small (order of mm) gaps at high voltage ( $> 10^4$ ) and the problem has been examined with respect to arcing in switches by Suits<sup>12</sup> some years ago. Here the discharge is probably initiated largely by electron current, with initial energies possibly comparable to the gap voltage, and subsequent vaporization of the electrodes from which a low degree of ionization results. With the formation of sufficient ionized vapor a "spark channel" is created<sup>13</sup> through which high currents may now pass; these processes can occur in times substantially shorter than 1  $\mu$ sec.

There is little presently known about the relative temperatures of ions and electrons during this early period. Presumably the electron temperature is initially very high; in column discharges Massey<sup>14</sup> reports  $w_e \gg w_i$ , as does Edels<sup>10</sup> for the particular case of low pressure discharges, but the times involved are very much longer than the duration of the experiments reported here.

It seems generally agreed that one can have some form of temperature equilibration in the order of milliseconds; distant coulomb collisions are effective for this purpose with high initial electron temperatures, as may be seen, for example, by the equipartition times given by Spitzer.<sup>15</sup> He gives the relation

$$t_{eq} = 5.9 \frac{AA_1}{n_1 z_1^2 z_1^2 \ln \Lambda} \left( \frac{T}{A} + \frac{T_1}{A_1} \right)^{3/2} \quad (1)$$

as the time for equipartition of energy for a test particle of mass number A among field particles  $A_1$ . In (1),  $\Lambda$  is the ratio of cut-off distance for interactions (Debye shielding distance) to the distance of closest approach, and  $\ln \Lambda$  is of the order of ten; T is in degrees Kelvin. In this case, one wants the equipartition time for high energy electrons found in the initial discharge to reduce to the ion temperatures (field particles). Thus

$$t_{eq} = 5.9 \times 10^5 \frac{A_1 A_e}{n_1 z_1^2} \left( \frac{w_e}{A_e} \right)^{3/2}, \quad (2)$$

since  $w_e/A_e \gg w_1/A_1$  if any reasonable value of  $w_e$  is chosen (w in eV). If, for example, one chooses  $w_1 = 120$  eV, and  $w_e = 1200$  eV,  $n_1 = 1.2 \times 10^{17}$ , and assume a Cu plasma ( $A_1 = 64$ ), substitution in (2) yields times of the order of 500  $\mu$ sec for  $z_1 = 1$  or 30  $\mu$ sec for  $z_1 = 4$ .

Ionization times, however, are considerably faster (as will be shown shortly) and one may suppose that the speedy attainment of low electron temperatures noted by Meek and Craggs<sup>13</sup> and others is due to a rapid increase in ionization level, with the initial hot electrons losing their energy by ionizing and heating bound electrons; the ion temperatures would, of course, be largely unaffected by this process. Suppose, for example, that during the early stage of the arc

formation  $w_e$  had reached a level of several kilovolts while the copper vapor was still largely singly ionized, and  $w_1 = 120$  eV (these conditions will be taken, for the moment, as entirely hypothetical in order to serve the computations which follow). The free electrons present would proceed to increase the ionization level, dropping in temperature, while losses through coulomb interactions with the ions would be negligible. The question arises, where would an equilibrium of some variety be achieved?

These plasmoids are optically thin so that the Saha equation is undoubtedly inapplicable. In 1952, Elwert<sup>16</sup> developed an equation for collision ionization - photorecombination equilibrium in the sun's corona:

$$\frac{N_{i+1}}{N_1} = \frac{S_{12}}{Q_{21}} = 8.3 \times 10^5 \frac{f_2}{f_1} \frac{L_n}{n^*g} \left( \frac{I_H}{I_1} \right)^2 \frac{\exp(-I_1/w_e)}{(I_1/w_e)}, \quad (3)$$

where

$\frac{N_{i+1}}{N_1}$  = relative prevalence of ion-(i + 1 ionized) vs ion-(i ionized),

$S_{12}$  = electron collision probability coefficient,

$Q_{21}$  = photorecombination coefficient,

$f_1/f_2$  = uncertainty factor  $\cong 9/8$ ,

$L_n$  = number of electrons in outermost occupied shell,

$n^*$  = principal quantum number of outermost shell,

$g$  = recombination probability factor for  $n^*$  or higher shells, a function of  $I_H(n^*)^2/w_e$  given in graphic form by Elwert.

If one takes



$$I_1 = \frac{(Z_{\text{eff}})^2}{(n^*)^2} I_H, \quad (4)$$

where  $Z_{\text{eff}}$  is the effective nuclear charge seen by the  $i^{\text{th}}$  electron and  $I_H$  is the ground state ionization potential of hydrogen (13.53 eV), and

$$s = \frac{I_1}{w_e}, \quad (5)$$

then combining (3), (4), and (5) yields

$$\frac{N_{i+1}}{N_1} = 9.4 \times 10^5 \frac{L_n}{n^* g} \left( \frac{I_H}{w_e} \right)^2 s^{-3} \exp(-s). \quad (6)$$

Suppose, now, one chooses  $w_e = 120$  eV at equilibrium (as was just hypothesized) and enquires as to the most prevalent ionized species of copper ( $Z = 29$ ). This may be determined by a trial-and-error process. For example, one finds that for  $i = z = 15$

$$\text{Cu(XV): } (1s)^2(2s)^2(2p)^6(3x)^4$$

$N_{16}/N_{15} = 1.4$  (the sub-states of the  $n^* = 3$  electrons are uncertain here). In this calculation, take  $Z_{\text{eff}} = 17.5$ ,  $n^* = 3$ ,  $L_n = 4$ , from which  $s = 3.85$ ,  $s(n^*)^2 = 34.6$ ,  $g = 4.3$  (from Elwert's graph). For  $i = z = 16$

$$\text{Cu(XVI): } (1s)^2(2s)^2(2p)^6(3x)^3$$

$N_{17}/N_{16} = 0.5$  ( $Z_{\text{eff}} = 18.5$ ,  $n^* = 3$ ,  $L_n = 3$ , from which  $s = 4.3$ ,

$s(n^*)^2 = 38.5$ ,  $g = 4.3$ ). Therefore, at  $w_e = 120$  eV the most prevalent specie is Cu(XVI), i.e.,  $z = 16$ .

Suppose the initial conditions before equilibration were as stated above, namely  $w_e > w_1$ , Cu(I) present. Then each electron would have to produce 15 ionizations, a total energy of (approximately)

$$I_H \sum_{z=2}^{16} \frac{z^2}{(n^*)^2} .$$

This may be estimated as 2100 eV. In addition, 1900 eV must be distributed among 16 electrons to produce 120 eV each. The initial electron must then have had about 4 keV. This is admittedly high.

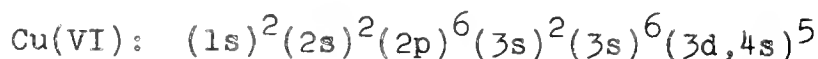
It is necessary also to show that the relaxation time for this process is sufficiently short, and this may be done utilizing an expression developed by Knorr<sup>17</sup> for corona equilibrium. Using symbols as defined above,

$$t = \frac{6.5 \times 10^5 (s w_e)^{3/2} \exp(s)}{L_n n_e} \quad (7)$$

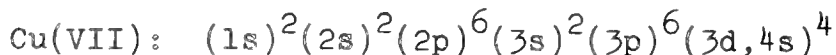
where  $n_e$ , the electron number density, is given by  $z n_1$ . For Cu(XVI),  $s = 4.3$ ,  $w_e = 120$  eV,  $L_n = 3$ , and  $n_e = (16)(2.7 \times 10^{15})$ . Substitution of these values in (7) yields  $t = 4.3$   $\mu$ sec which is of the order of the experiment time. It is likely to be an upper bound, however, since (7) is constructed primarily for an examination of equilibration time for electron energies close to final equilibrium. But in the process suggested here the initial

electron temperature would be considerably higher, and equilibrium would be attained at a faster rate.

An initial electron temperature of 4 keV is difficult to accept, although there might well be a small proportion of "runaway" electrons produced in the initial discharge. However, their thermalization would depend upon a rapid increase in electron scattering as the spark becomes pinched prior to its propulsion down the tube. It is likely that the electron temperature is initially one to two orders of magnitude smaller. Consider, for example, a corona equilibrium at  $w_e = 12$  eV. For  $i = z = 6$



$N_7/N_6 = 5.4$  using (6). The quantum states of the five outer electrons are uncertain but the 3d and 4s levels should be sufficiently close so that ionization from either is equivalently weighted. For this computation, take  $Z_{\text{eff}} = 7.5$ ,  $n^* = 3.3$ ,  $L_n = 5$ , from which  $s = 5.75$ ,  $s(n^*)^2 = 63$ ,  $g = 5.3$ . For  $i = z = 7$



$N_8/N_7 = 0.9$  (taking  $Z_{\text{eff}} = 8.5$ ,  $n^* = 3.5$ ,  $L_n = 4$ , from which  $s = 6.75$ ,  $s(n^*)^2 = 81$ ,  $g = 5.7$ ). Thus, the prevalent species at  $w_e = 12$  eV is Cu(VII), i.e.,  $z = 7$ .

If initial conditions before this equilibrium were, again, that  $w_e > 12$  eV, Cu(I) prominent, then each electron would have to produce 6 ionizations for a total energy of (approximately)

$$I_H \sum_{z=2}^7 \frac{z^2}{(n^*)^2} \quad .$$

This may be estimated as 175 eV. In addition, 85 eV must be distributed among 7 electrons to produce 12 eV each. The initial electron must then have had about 260 eV, or about twice the ion temperature. This is, perhaps, a more reasonable initial condition.

The relaxation time for this process should be tested, also. Using the above parameters for Cu(VII), with  $n_e = (7)(2.7 \times 10^{15})$ , (7) gives  $t = 5.4 \mu\text{sec}$ . This is again of the time order of the experiment and should be considered an upper bound for the reasons previously stated.

For the purposes of understanding the origin of the high ion temperatures suggested by the data, one may speculate on a mechanism whereby the plasmoid might acquire a thermal energy comparable to its energy of axial motion. Experience with discharge phenomena suggests that the initial ion temperature may have been no more than a few electron volts.<sup>10</sup> However, it is probable that the spark channel pinches during current passage.<sup>5</sup> The effect upon the sub-burst is to blow it outward, down the tube, and might be likened to the sub-burst being hit by a fast-moving wall. This creates a shock wave in the gas, and a significant fraction of the axial kinetic energy acquired from the pinch can thus be thermalized. In the limit of a strong shock in a polytropic gas this fraction can be approximated theoretically.<sup>18</sup> One writes

$$\frac{T_1}{T_0} = \mu^2 (1 + \mu^2) M_0^2 ,$$

where  $M_0$  is the initial Mach number, the subscripts refer to the states on either side of the shock, and

$$\mu^2 = \frac{\gamma - 1}{\gamma + 1} .$$

For this discussion take  $\gamma = 5/3$ ,  $\mu = 1/2$ . If one assumes (as has been done here) that the axial velocity imparted to the plasmoid is approximately that of the moving wall (the shock), then  $M_0 = v_a/c$ , with  $c$  the sound speed in the unperturbed spark channel. But one has

$$c^2 = \gamma R' T_0 ,$$

where  $R'$  is the gas constant per unit mass, which results in

$$T_1 = \frac{\mu^2 (1 + \mu^2)}{\gamma} \frac{v_a^2}{R'} .$$

Now  $(3/2)R'T_1$  is the final thermal energy per unit mass, acquired from interaction with the shock, of which the ions acquire half, i.e.,  $T_1 = (2/3)v_{ta}^2/R'$ . Therefore, one obtains

$$\left( \frac{v_{ta}}{v_a} \right)^2 = \frac{3\mu^2 (1 + \mu^2)}{2\gamma} = 0.28 .$$

Insofar as the endothermic reactions behind the shock have been neglected (increase in degree of ionization) this is an

overestimate. Experimentally, for the leading sub-burst  
 $(v_{ta}/v_a)^2 = 0.11$ .

One may also show that bremsstrahlung is not an appreciable energy loss for these plasmoids. Taking the power loss per unit volume given by Spitzer<sup>15</sup> as (emu)

$$1.4 \times 10^{-27} z^3 n_1^2 T_1^{1/2},$$

one obtains for the energy loss per electron during the course of the experiment (12  $\mu$ sec)

$$\Delta w = 1.05 \times 10^{-21} z^2 n_1 T_1^{1/2} \text{ eV.}$$

An upper bound is obtained by taking  $z = 16$ ,  $n_1 = 2.7 \times 10^{15}$ ,  $T = 1.2 \times 10^6$ , from which  $\Delta w = 0.8$  eV per electron.

With these possible values of  $z$  (depending upon assumed initial conditions), theoretical estimates may now be made of the plasma drift velocity, and compared to the observed expansion of the plasmoid flow in region c., as described in Section 1, above. There, a one percent lateral drift was noted. If  $v_{||} = 5.5 \times 10^6$  cm/sec, then the expectation is that  $v_{\perp} = 5 \times 10^4$  cm/sec.

There are, unfortunately, two non-equivalent drift proposals from which to choose at the present time. The now classical interpretation is that complete transverse confinement is dependent upon infinite plasma conductivity, with lateral drift being proportional to  $\bar{E} \times \bar{B}$  (the electric field resulting from

resistance within the plasma), the result of electron-ion collisions. This leads to an expression<sup>15</sup> (emu)

$$v_{\perp} = \frac{1.3 \times 10^{13}}{B^2 T_1^{3/2}} \frac{z \ln \Lambda}{|\nabla p|} \quad (8)$$

Conversely, Bohm, Burhop, and Massey<sup>19</sup> have proposed (without proof) that drift in the presence of a magnetic field is a "drain" mechanism, a consequence of the crossed electric fields caused by plasma oscillations, and that the drift velocity is given by<sup>15</sup> (emu)

$$v_{\perp} = \frac{3.9 \times 10^{18}}{B n_e} |\nabla p| \quad (9)$$

It is interesting to note that, aside from a difference in dependence on field strength, (8) is proportional to  $z/T^{1/2}$  while (9) depends implicitly on  $T/z$  (noting that  $n_e = z n_i$ ). Purported experimental verifications for both (8) and (9) have been recently presented, respectively, by Simon<sup>20</sup> and by Lehnert.<sup>21</sup>

Proceeding now to apply these expressions to the present case, an estimate of  $\nabla p$  is required. An upper bound for the average pressure is

$$p = n_i k T_i \quad .$$

If one assumes a circular cross-section for the plasmoid and a linear (radial) pressure gradient, then it can be easily shown

that

$$p_{\max} = 3p = 3n_1 kT_1 .$$

The plasmoid diameter is about 1.5 cm, from which

$$|\nabla p| = \frac{p_{\max}}{0.75} = 4n_1 kT_1 . \quad (10)$$

Consider, first, the electron-ion collision mechanism. With  $\ln \Lambda = 10$ ,  $B = 1.1 \times 10^4$ ,  $n_1 = 2.7 \times 10^{15}$ ,  $T_1 = 1.2 \times 10^6$ , one obtains from (8) and (10)  $v_{\perp} = 1.5 \times 10^3 z$  cm/sec. If a very high initial electron temperature is assumed, as above, perhaps  $z = 16$ , and  $v_{\perp} = 2.4 \times 10^4$  cm/sec. This is not unreasonable in comparison to an experimental value of  $5 \times 10^4$  cm/sec. But it is seen that, for this mechanism, any assumption of lower  $z$  increases the discrepancy.

Employing the Bohm proposal, a combination of (9) and (10), with parameters as before, yields  $v_{\perp} = (2.4 \times 10^5 / z)$  cm/sec; If  $z = 16$ ,  $v_{\perp} = 1.5 \times 10^4$  cm/sec, if  $z = 7$ ,  $v_{\perp} = 3.5 \times 10^4$  cm/sec, the latter being closer to observation. It is seen, incidentally, that the Bohm drift velocity will not, in general, be much the larger in strong magnetic fields except in the special case of fusion interest, namely, a hydrogenic plasma at moderate density and very high temperature.

One may now calculate, also, a range of possible ion Larmor radii. Using (emu)

$$r = \frac{Mv_{\perp}}{Bze},$$



a measure of  $r$  may be obtained for the a. and c. regions. If  $M = 64$  a.m.u. in grams,  $v_{ta} = 1.9 \times 10^6$  cm/sec,  $B = 1.1 \times 10^4$  emu,  $z = 7$ , then  $r = 0.17$  cm. This will be reduced to  $r = 0.08$  cm for region b. Any higher value for  $z$  and/or lower ion temperature will reduce these figures accordingly. In any case, they are substantially smaller than the plasmoid dimensions and any distance of appreciable variation in  $B$ .

Another question of interest concerns the interaction between the plasmoid ions and the "mirror" separating regions a. and b. in the normal Differential Solenoid. The effect of a magnetic mirror geometry is well known in problems of plasma confinement; it depends upon the fact that the magnetic moment of the individual ion in a helical path,  $\mu = ev_{\perp}r/2$ , is an adiabatic invariant of the motion (if  $B_z$  is constant over  $r$ ), so that a positive  $B_z$  gradient behaves like a potential barrier. The particle thus gains transverse kinetic energy,  $w_{\perp}$ , as the Larmor radius decreases, which by conservation it obtains from the axial kinetic energy. If the mirror ratio,  $R = B_b/B_a$ , is sufficiently large, the particle is reflected;<sup>22</sup> the critical angle for reflection<sup>15</sup> is  $\sin^2 \theta = 1/R$ . This analysis can be extended to a dynamical plasma, i.e., a plasmoid with a c.m. velocity along the axis, with rather interesting results. In particular, in the limit of zero c.m. velocity it will be shown that the reflection coefficient is  $F_r = (1-1/R)^{1/2}$ . This total reflection coefficient is the fraction of the entire ion population in the plasmoid ultimately reflected, and should not be confused with the  $1-1/R$  of Spitzer, which is the

fraction of the incident ions reflected per unit time.

To reformulate, total kinetic energy is conserved:

$$dw_{||} + dw_{\perp} = 0, \quad (11)$$

where  $w_{||}$  and  $w_{\perp}$  refer to axial and rotational kinetic energy.

If  $\mu$  is an invariant, then one may write

$$dw_{\perp} = \mu dB. \quad (12)$$

Combining (11) and (12), one obtains

$$\frac{dw_{||}}{dz} + \mu \frac{dB}{dz} = 0, \quad (13)$$

where  $w_{||}$  and  $B$  may be assumed (for simplicity) to have only  $z$  components which, in turn, have only  $z$  gradients. The first term of (13) may be integrated as a force decreasing the axial velocity, so that

$$\begin{aligned} F_z &= M \frac{dv_{||}}{dt} = \frac{dw_{||}}{dz} \\ &= -\mu \frac{dB}{dz}. \end{aligned} \quad (14)$$

In the simplest case, all differentials can be taken as linear variations, yielding

$$M \frac{\Delta v_{||}}{\Delta t} = -\mu \frac{\Delta B}{\Delta z}. \quad (15)$$

Take the plasmoid to consist of  $N$  ions (and associated electrons) having an isotropic Maxwellian velocity distribution,

$f(v)$ , with respect to the c.m., and with a c.m. speed  $\mathcal{U}$ , the direction of which defines the axis. A fraction of the ions,  $dN/N$ , will possess a speed in the range  $v$  and  $v+dv$ , and thus will lie on the surface of a sphere of radius  $v$  in velocity space, with axis parallel to the c.m. motion. In the moving frame of the c.m. motion, furthermore, the  $\bar{v}$  of every ion contained in  $dN$  will lie on some cone of revolution with angle  $\alpha$  to the axis ( $0 \leq \alpha \leq \pi$ ). We now enquire what fraction,  $f_r^v$ , of the  $dN$  ions with velocity  $\bar{v}$  will be reflected as a consequence of their orientation, when the plasmoid enters the magnetic mirror.

First, take

$$v_{\perp} = v \sin \alpha, \quad (16)$$

$$v_{\parallel} = \mathcal{U} + v \cos \alpha. \quad (17)$$

The expression for  $\mu$  can now be written

$$\mu = \frac{evr}{2} \sin \alpha \quad (18)$$

from (16). Combining (15) with (18), one obtains

$$\sin \alpha = - \frac{2M\Delta v_{\parallel} \Delta z}{evr\Delta t \Delta B}. \quad (19)$$

If the particle is to be stopped,  $\Delta v_{\parallel} = -v_{\parallel}$ . If the particle is experiencing uniform deceleration,  $\Delta z/\Delta t = v_{\parallel}/2$ . Also, one may write  $\Delta B = (R-1)B_a$ . Substituting in (19), one obtains

$$\sin \alpha = \frac{M(v_{\parallel})^2}{evB_a(R-1)} . \quad (20)$$

However, there is also the relationship

$$B_a e r = M v_{\perp} = M v \sin \alpha . \quad (21)$$

Combining (17), (20), and (21) yields

$$u/v = (R-1)^{1/2} \sin \alpha - \cos \alpha . \quad (22)$$

(The result may be obtained also by transforming  $\sin^2 \theta = 1/R$  to a coordinate system moving with the c.m.) This result, (22), may be plotted as the speed ratio,  $S = u/u$ , versus  $\alpha$ , a family of curves in  $R$ . Figure 19 shows curves for several  $R$ , as noted. It is convenient to solve (22) for  $\cos \alpha$ , yielding

$$\begin{aligned} \cos \alpha &= -\frac{1}{Rv} \pm \left\{ \left[ \frac{1}{R} \left( \frac{u}{v} \right)^2 - 1 \right] \left[ \frac{1}{R} - 1 \right] \right\}^{1/2} \\ &= -\frac{u}{Rv} \pm \left[ b \left( 1 - \frac{a}{v^2} \right) \right]^{1/2} , \end{aligned} \quad (23)$$

where

$$a \equiv \frac{u^2}{R} , \quad b \equiv 1 - \frac{1}{R} . \quad (24)$$

This double-valued function, (23), defines the angular limits  $\alpha_1$  and  $\alpha_2$ , between which an ion with velocity  $\bar{v}$  must lie in order to be reflected; if one takes the positive sign to correspond to  $\alpha_1$ , then  $0 \leq \alpha_1 \leq \alpha_2 \leq \pi$ . For a given mirror ratio,  $R$ , and axial speed,  $u$ , a pair of angles for reflection are defined only down to some minimum value of  $v$ , at and below which no orientation will provide reflection. One sees from (23) that

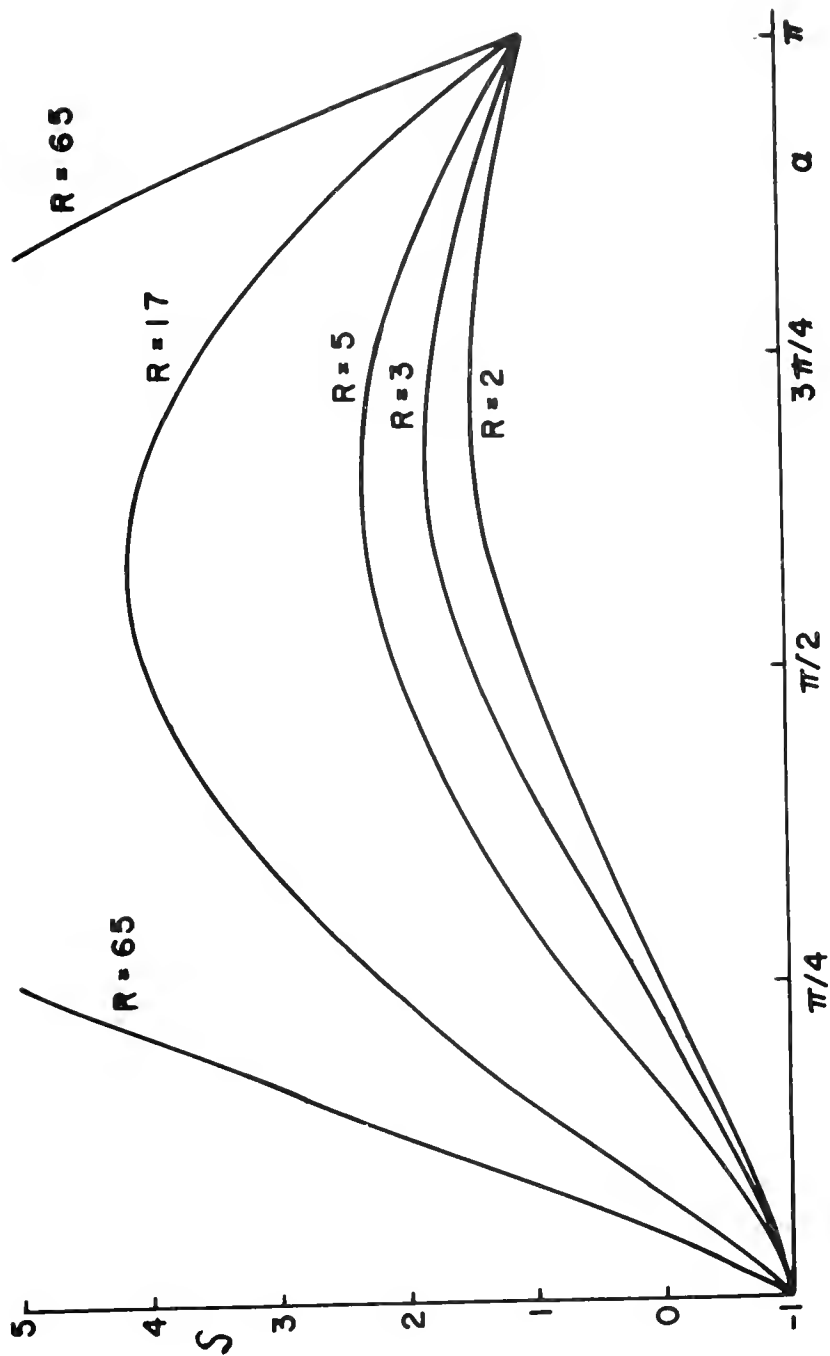


Figure 19  
Effectiveness of Magnetic Mirror for Variation of Particle  
Velocity Orientation in Moving Plasmoid



this minimum value is  $v = a^{1/2}$  for which a single  $\alpha$  is defined,  $\cos \alpha = -1/R^{1/2}$ . Every spherical velocity shell with  $v > a^{1/2}$  will contain a band of ions, bounded by latitudes at  $\alpha_1$  and  $\alpha_2$ , which will be reflected. The fraction which these reflected ions bear to the total ions of any given shell,  $dN$ , is just the ratio of the bounded area on the shell to the total area. One may show readily that this ratio is  $(\cos \alpha_1 - \cos \alpha_2)/2$ . Therefore,

$$f_r^v = f_1 = 0 \quad ; \quad v \leq a^{1/2} \quad (25)$$

$$\begin{aligned} &= f_2 = (\cos \alpha_1 - \cos \alpha_2)/2 \\ &= [b(1 - \frac{a}{v^2})]^{1/2} \quad ; \quad v \geq a^{1/2} \end{aligned} \quad (26)$$

based upon the above arguments and (23).

The Maxwellian velocity distribution is

$$\begin{aligned} \frac{dN}{N} &= 4\pi \left(\frac{M}{2\pi kT}\right)^{3/2} \exp(-Mv^2/2kT) v^2 dv \\ &= (16c^3/\pi)^{1/2} \exp(-cv^2) v^2 dv, \end{aligned} \quad (27)$$

where

$$c \equiv M/2kT. \quad (28)$$

The total fraction,  $F_r$ , of the ions reflected is then

$$\begin{aligned} F_r &= \int_N \frac{f_r^v dN}{N} \\ &= \int_{N(v \geq a^{1/2})} \frac{f_2 dN}{N}, \end{aligned} \quad (29)$$

from (26). Combining the integral of (29) with (27) yields

$$\begin{aligned}
 F_r &= \int_a^\infty \left[ b \left( 1 - \frac{a}{v^2} \right) \right]^{1/2} \left[ \frac{16c^3}{\pi} \right]^{1/2} \exp(-cv^2) v^2 dv \\
 &= \left( \frac{4bc^3}{\pi} \right)^{1/2} \int_a^\infty (v^2 - a)^{1/2} \exp(-cv^2) d(v^2) \quad (30') \\
 &= b^{1/2} \exp(-c/a). \quad (30)
 \end{aligned}$$

(By adopting the transformation  $y = (v^2 - a)^{1/2}$ , (30') may be converted to integrable form.) Now, applying (24) and (28) to (30) yields

$$F_r = (1 - 1/R)^{1/2} \exp(-M\mathcal{U}^2/2kTR). \quad (31)$$

Now apply this result to the present data. A lower bound for the ratio of axial to thermal energy (vide supra) for the leading peak, L, is given by  $(v_a/v_{ta})^2 = 9.3$ , and this may be equated to  $(2/3)(M\mathcal{U}^2/2kT)$ . The mirror ratio was  $R = 2.5/1.1 = 2.3$ . Therefore, from (31),  $F_r = 0.0017$ , or essentially no portion of L was reflected. A similar analysis for the trailing peak, T, gives  $F_r = 0.11$ , which is substantially larger, but it is problematical whether the effect was photographically recordable. If one associates with the T peak the hazy light surrounding the central beam in region a. of Figure 14c., then it does appear as if a noticeable fraction of these ions is missing in region b.

There is a possible extension of these calculations which



may be suggested here. The above analysis was designed to investigate the possibility of stopping completely certain ions with appropriate velocity orientation. In fact, even if an ion is not stopped it will experience some deceleration by the mirror. A more general solution might thus be made to yield the redistribution of velocities occasioned by mirror transit of the plasmoid, based on an initial isotropic Maxwellian distribution.

### C. Plasmoid Flow in the Shorted Differential Solenoid:

The axial values of magnetic induction are given, in each case below, for regions a. and c. and for region b. (see Figure 7). The field intensity in region b. decreased radially about 25 per cent at the wall, as is described in Section IIE2, while the jumpers contributed a relatively strong transverse field. The source was fired at 12 kV, producing 40 joules. The pictures which follow are again individual bursts, taken with open shutter and appropriate apertures, and are representative and reproducible. Synchronization was arranged to place the plasmoid burst approximately 10 cm into region a. at maximum field.

Figure 20 shows the flow pattern of the plasmoid in two camera views. In 20a. is seen the position of the jumper, with the wires of the second jumper cut and extending from behind the solenoid. There is clear collimation into region b., where the plasmoid immediately expands to the walls of the tube, as do the field lines, and is then recollimated in region c. (Figure 20b.)

Considerable turbulence is suggested by Figure 20c., with a noticeable dark area along the bottom of region b. This is the side on which the jumper is located;  $B_z$  at the wall in the center of region b. is approximately  $0.3 \text{ weber/m}^2$  while the transverse field from the jumper is about  $0.5 \text{ weber/m}^2$ , so that  $\bar{B}$  has a strong azimuthal orientation.

To investigate this effect further, a second jumper was placed across the opposite side of region b. This would be expected to halve the transverse field toward the edge of the tube near the first jumper and spread it more uniformly across region b. The somewhat surprising result is shown in Figure 21, where the incoming plasmoid has been diverted to one side of region b. However, it will be noted that the emergent beam has remained unaltered.

D. Plasmoid Flow in the Curved Solenoid: This geometry was shown in Figure 9, Section IIF, and discussed there. The mean value of the magnetic induction,  $B_z$ , is given in each case below, as determined by the initial bank voltage. The plasmoid source was fired at 3, 6, and 12 kV, yielding 2.5, 10, and 40 joules, respectively, as noted. Photographs were taken with shutter open, at appropriate aperture, of single bursts, except as noted. The results shown here are representative and reproducible.

Figure 22 shows plasmoid flow for two values of mean  $B_z$  and plasmoid at 40 joules. The interesting result is seen that doubling of field intensity appears to cause no alteration in the flow path; in both cases the plasmoid is initially collimated but



Solenoid<sup>20a.</sup>



<sup>20b.</sup>  
 Plasma: 40 joules  
 Regions a. and c.:  
     1.3 webers/m<sup>2</sup>  
 Region b.(axis):  
     0.41 weber/m<sup>2</sup>

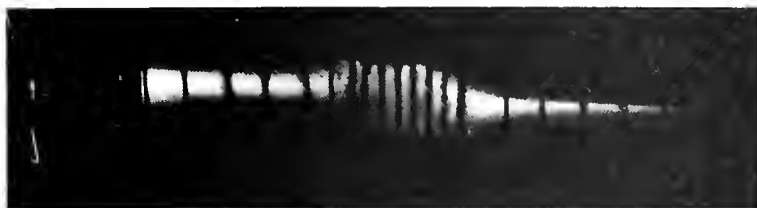


<sup>20c.</sup>  
 (Same as 20b.)

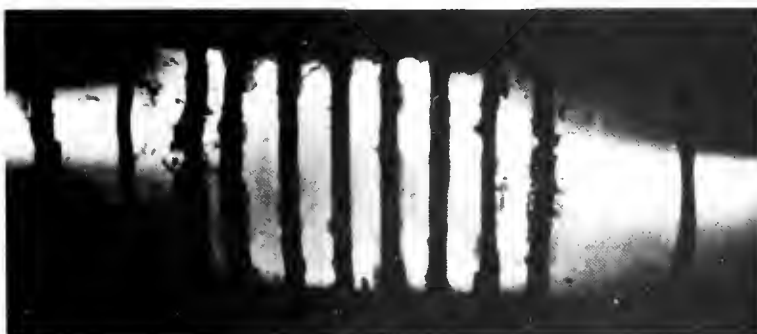
Figure 20

Plasmoid Flow in the Shorted Differential Solenoid.  
 I. Single Jumper





21a.  
 Plasma: 40 joules  
 Regions a. and c.:  
     1.3 webers/m<sup>2</sup>  
 Region b. (axis):  
     0.41 weber/m<sup>2</sup>

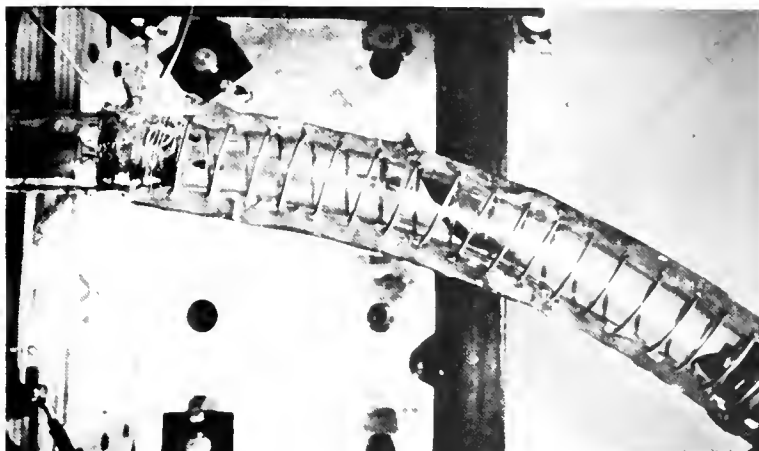


21b.  
 (Same as 21a.)

Figure 21

Plasmoid Flow in the Shorted Differential Solenoid.  
 II. Double Jumper





22a.  
Solenoid



22b.  
No field



22c.  
 $B_z: 1.4 \text{ webers/m}^2$



22d.  
 $B_z: 2.8 \text{ webers/m}^2$

Figure 22

Plasmoid Flow in the Curved Solenoid.  
I. Plasmoid at 40 joules





moves into the tube wall at about the sixth (visible) solenoid turn, evidencing little transverse confinement. Beyond this point, the plasmoid presumably flows along the outer inside wall of the tube. The fact that doubling the field intensity produces no visible effect suggests that the overriding processes contributing to non-confinement are not single particle but collective, i.e., the density is sufficiently high so that single particle mechanisms are not substantially operative.

With this in mind, the experiment was repeated with the plasma source capacitor energized to half the voltage, 6 kV, producing a 10 joule burst. This was expected to produce some unspecified decrease in center-of-mass velocity and temperature in addition to quartering the density. The results are seen in Figure 23. One now notes a distinct improvement in transverse confinement at  $1.4 \text{ weber/m}^2$  and a further improvement when the field was doubled.

Finally, the source capacitor voltage was again halved, with the results shown in Figure 24. Here confinement is quite good, although a portion of the residual plasma continues to travel (and recombine) along the outer wall.

Perhaps the least sophisticated analysis that could be applied to these results would be that of comparing field and plasmoid energy density since confinement implies that the former exceeds the latter, i.e.,  $\beta < 1$ . For the case of the plasmoid fired from the source energized to 40 joules (the usual arrangement in this study) mass density has been estimated at  $2.9 \times 10^{-4} \text{ kg/m}^3$  and maximum velocity at  $5.5 \times 10^4 \text{ m/sec}$ , from

which the plasmoid translational energy density is about  $4.4 \times 10^5$  joules/m<sup>3</sup>. With magnetic induction at 1.4 weber/m<sup>2</sup>, field energy density is somewhat higher, at  $7.8 \times 10^5$  joules/m<sup>3</sup>, yet confinement was not observed. In addition, some visible improvement should have resulted from increasing field energy density to  $3.1 \times 10^6$  joules/m<sup>3</sup> (doubling solenoid voltage), but Figures 22c. and d. suggest otherwise.

At the other extreme one knows theoretically that single particles should experience transverse confinement under appropriate conditions, namely those which result in drift velocities substantially smaller than the axial velocity. Single-particle drift in this geometry will result both from a transverse field gradient,  $\nabla_{\perp} B$ , (such as is present in a curved field) and from centrifugal force. These two velocities are given, respectively, by

$$v_d' = \frac{rv_{\perp}}{2R} \quad \left( \frac{\nabla_{\perp} B}{B} \approx \frac{1}{R} \right) \quad (32)$$

and by

$$v_d'' = \frac{v_{\parallel}^2}{R\omega}, \quad (33)$$

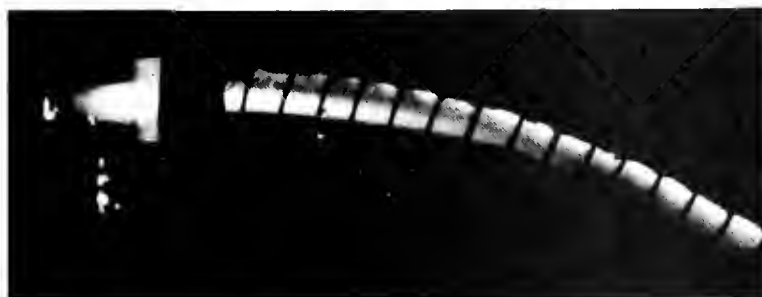
where  $r$  is the Larmor radius,  $R$  the radius of curvature of the solenoid,  $\omega$  the cyclotron frequency, and  $v_{\perp}$  and  $v_{\parallel}$  the transverse and longitudinal ion velocities, respectively. Of these two,  $v_d''$  is much the larger for the present experimental parameters (and  $v_d''$  for electrons is negligible). Confinement therefore implies that  $v_d'' \ll v_{\parallel}$ , which by (33) is equivalent to requiring



23a.  
No field



23b.  
 $B_z: 1.4 \text{ webers/m}^2$



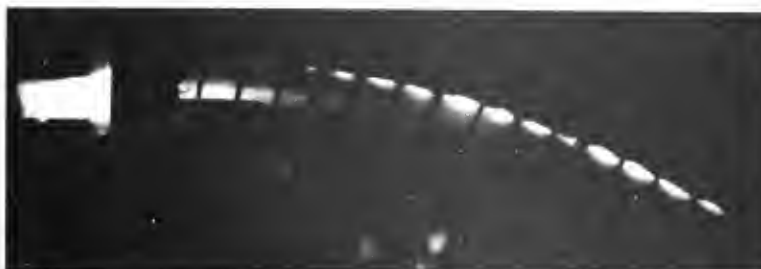
23c.  
 $B_z: 2.8 \text{ webers/m}^2$

Figure 23  
Plasmoid Flow in the Curved Solenoid.  
II. Plasmoid at 10 joules

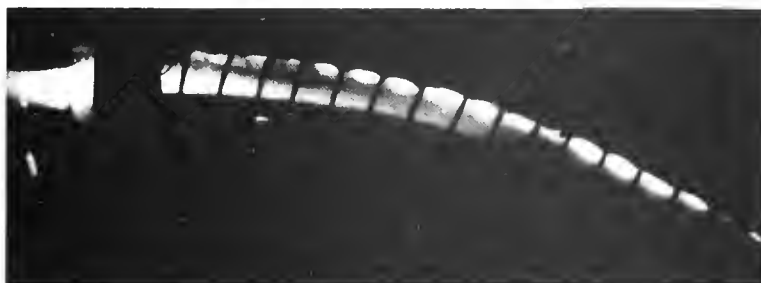




24a.  
No field  
(triple shot)



24b.  
 $B_z: 1.4 \text{ webers/m}^2$   
(double shot)



24c.  
 $B_z: 2.8 \text{ webers/m}^2$

Figure 24

Plasmoid Flow in the Curved Solenoid.  
III. Plasmoid at 2.5 joules



that  $v_{||} \ll R\omega = (R/r)r\omega = (R/r)v_{\perp}$ . Since  $v_{||} \approx 3 v_{\perp}$  while  $R \gg r$ , the condition is clearly satisfied: had the plasmoid a sufficiently low density, it would follow the field lines.

On the other hand a sufficiently dense plasmoid will develop a polarization electric field, as the result of charge separation created by  $v_d''$ , which will result in an  $\bar{E} \times \bar{B}$  radial drift of almost the magnitude needed to compensate for the field curvature. The plasmoid will thus travel in a nearly straight line, at an increasing inclination to the field. A similar effect was seen in the experiments of Bostick,<sup>3</sup> where plasmoid velocity was perpendicular to the field. To study this (the following argument was kindly suggested by Professor George Schmidt of Stevens Institute of Technology), adopt a rotating coordinate system (traveling with the plasmoid) of angular velocity  $v_{||}/R$ . The charge separation drift,  $v_d''$ , creates an electric displacement,  $\bar{D}$ , which increases at the rate

$$\dot{\bar{D}} = qn\bar{v}_d + \epsilon_0 \dot{\bar{E}}, \quad (34)$$

with  $q$  the charge per ion and  $n$  the number density. Now assume the condition (to be shortly verified) that

$$\epsilon \gg \epsilon_0, \quad (35)$$

so that the second term to the right in (34) becomes negligible. Also, since the polarizability,  $\epsilon - \epsilon_0$ , of the plasmoid may be taken as<sup>15</sup>  $Mn/B^2$  (with  $M$  the ion mass), it follows from (35) that

$$\epsilon = Mn/B^2. \quad (36)$$

Now, the radial drift,  $\bar{v}_r = \bar{E} \times \bar{B}/B^2$  will increase at the rate

$$\dot{\bar{v}}_r = \dot{\bar{E}} \times \bar{B}/B^2 = \dot{\bar{D}} \times \bar{B}/\epsilon B^2. \quad (37)$$

If one combines (33) through (37), he obtains

$$\dot{\bar{v}}_r = v_d'' \omega = v_{||}^2/R$$

which implies rectilinear motion in the laboratory frame.

However, if the plasmoid is traveling through a conducting background, circulating external currents are created (through the background) which reduce the polarization field in the laboratory frame. Indeed, if the background medium remains at rest, leaving the plasmoid moving only in the magnetic field, the plasmoid will now follow the field closely (providing, further, that the plasmoid pressure is small compared to  $B^2/2\mu_0$ , the  $\beta \ll 1$  condition).

The conditions, then, for rectilinear motion are a vacuum region surrounding the plasmoid and (35) (which may be seen to be equivalent to  $Mnc^2 \gg B^2/2\mu_0$ ). For the present experiment, taking  $M \sim 60$  a.m.u. and  $B = 2$  weber/m<sup>2</sup>, one finds that (35) and (36) imply that  $n \gg 3 \times 10^8$  ions/cm<sup>3</sup> which is well-satisfied (Section IIIB3). However, in some results, e.g., Figure 24, an earlier portion of the plasmoid, traveling rectilinearly into the wall, may have created the necessary background atmosphere for permitting later portions to follow the field, in the manner described in the previous paragraph. The results of Figure 22 and the slight effect of doubling the field noted in Figure 23 probably relate to poor satisfaction of the  $\beta$  condition.



## APPENDIX I

### Experimental Equipment

This section describes the overall arrangement of experimental equipment. The Appendices which follow will provide details on the various components.

Figure 25a. shows the Differential Solenoid emplaced upon the plasma source capacitor; the leads to the search coil may be seen. Behind is the solenoid capacitor bank and to the left the ignitron unit. In the left foreground is the control console including the pulse and waveform generators. Vacuum equipment is to the right, off the picture. Figure 25b. is a closer view. Here, the main vacuum system is in the background, right. In the foreground is the button source trigger to the spark gap of the main (coaxial) source, together with the vacuum arm (coming forward and up) to the auxiliary vacuum system, off the picture to the right.

A direct view of the trigger system is given in Figure 26. The cross of the T is the button source trigger, with capacitor at right. The vacuum line comes off forward. At left is a top view of the capacitor for the coaxial plasma source which is mounted above it.

Figure 27 gives two views of the Curved Solenoid. Here the button source assembly is covered with photographer's cloth as in an actual run (to block spurious light to the camera). The search coil is clearly seen.

The entire experimental arrangement is shown schematically in Figure 28. The main power supply, control unit, ignitron unit, and pulse amplifier were designed and built in this laboratory and are described in Appendix IV. The coaxial plasma source was also original and is described in Appendix II. The trigger ("ion gun"), usually a button or rail source, is described in Appendix III. The main vacuum system (6") was a commercially assembled unit (Kinney Model PW-600); the auxiliary system (2") was laboratory assembled around a commercial diffusion pump (CVC Model MCF-60). The 5 kV supply was a laboratory assembled half-wave rectifier with a 2 kVA transformer, and some filtering to counteract the small time constant associated with the trigger capacitor. The 12 kV supply was a commercial 30 kV, 2mA unit (Beta, Model 202/R). The main capacitor bank was described in Section IIC. The pulse and sawtooth generators were commercial units (Tektronix, Models 161 and 162, respectively).

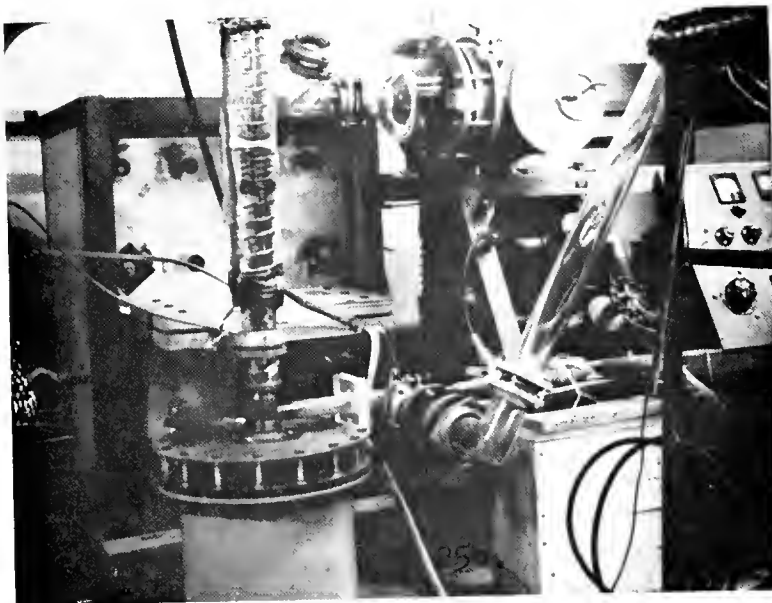
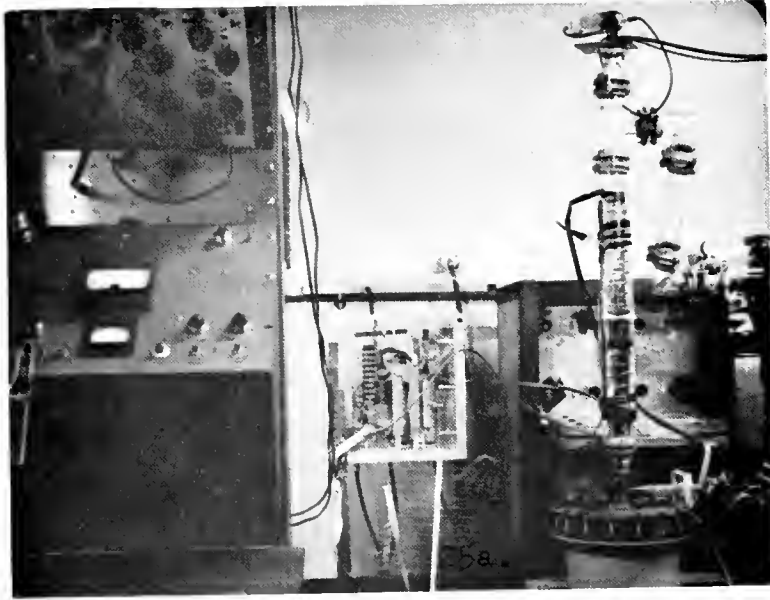


Figure 25

Experimental Arrangement with Differential Solenoid



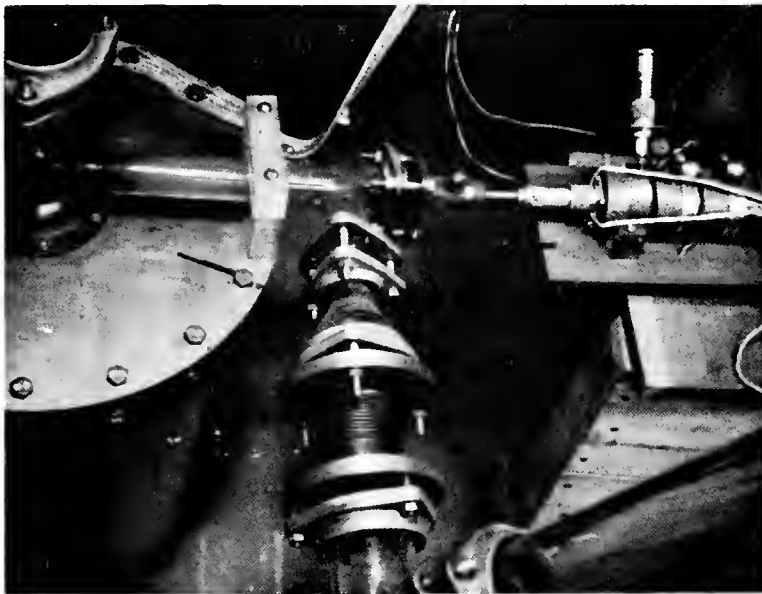
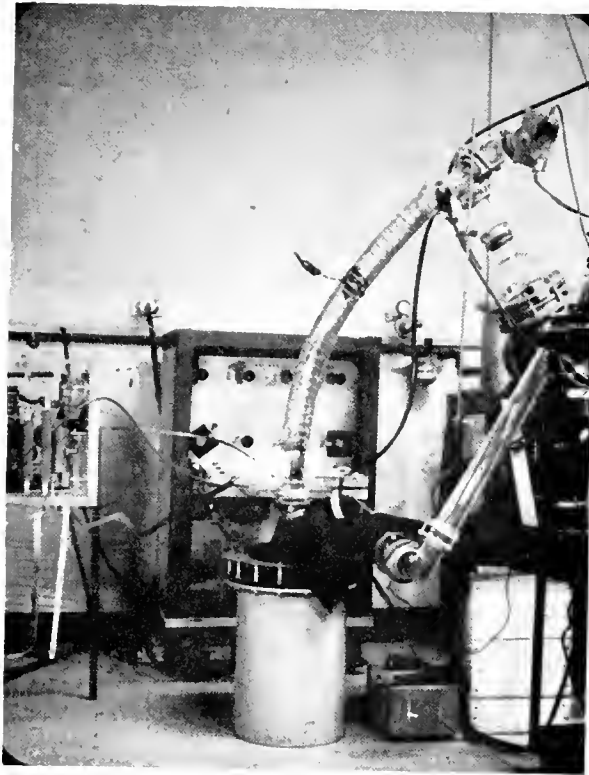
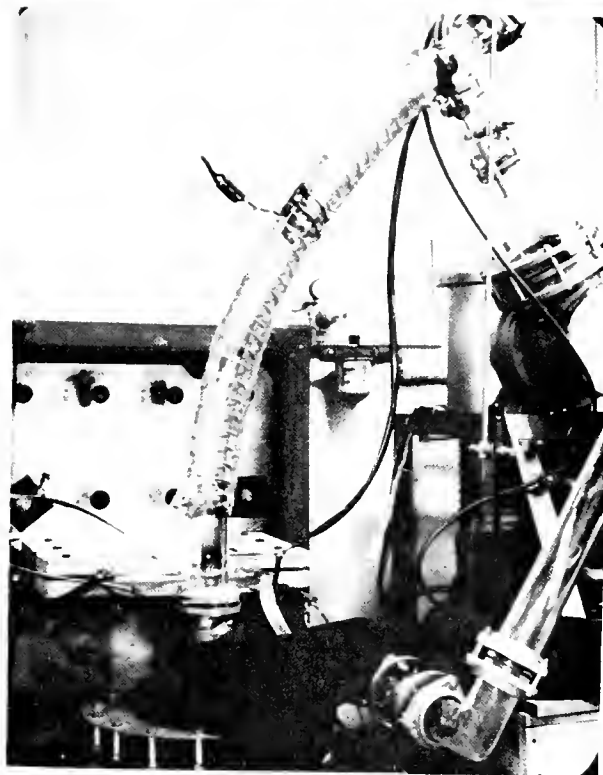


Figure 26  
Button Source Trigger





27a.



27b.

Figure 27  
Experimental Arrangement with Curved Solenoid









## APPENDIX II

### Coaxial Plasma Source

The main source for the experiments was a pair of coaxial, brass electrodes, employing the "shaped charge" geometry. Design details are seen in Figure 29. The center terminals of the firing capacitor were fastened through a cylindrical brass block, out of which projected the bottom electrode of the trigger spark gap. The upper electrode of the spark gap and the center electrode of the plasma source were connected and seated in Teflon. The return path of the outer plasma electrode was along a section of 2" brass pipe (appropriately slotted) which was seated on a circular copper plate connected to the ground terminals of the capacitor.

### APPENDIX III

#### Button Source Trigger

The trigger for the vacuum spark gap switch of Figure 29 is shown in Figure 26, inserted into the cross-bar of the T, with its own coaxial capacitor on the right. A detail of this arrangement is shown in Figure 30 (where, in this drawing, the source was shown coaxial). The capacitor was a hollow cylinder of barium titanate, silvered on the inner and outer surfaces. Trigger was air gap from the pulse amplifier (see Appendix IV). This figure shows the arrangement which was actually employed as the main plasma source of earlier experiments;<sup>1</sup> when the larger coaxial source was constructed (Appendix II), a button gun was substituted on this device and it was employed as the spark gap trigger.

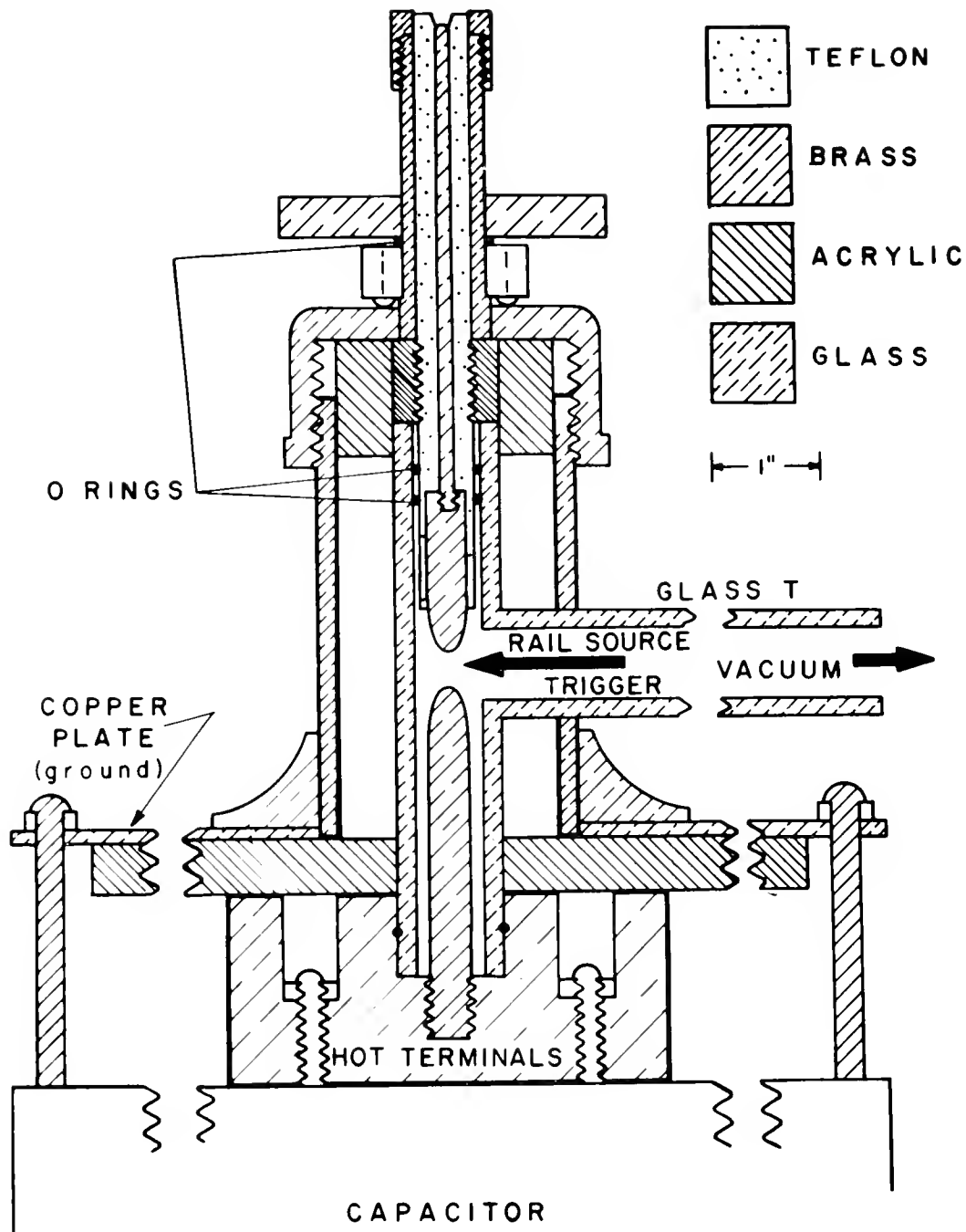


Figure 29  
Detail of Coaxial Plasma Source



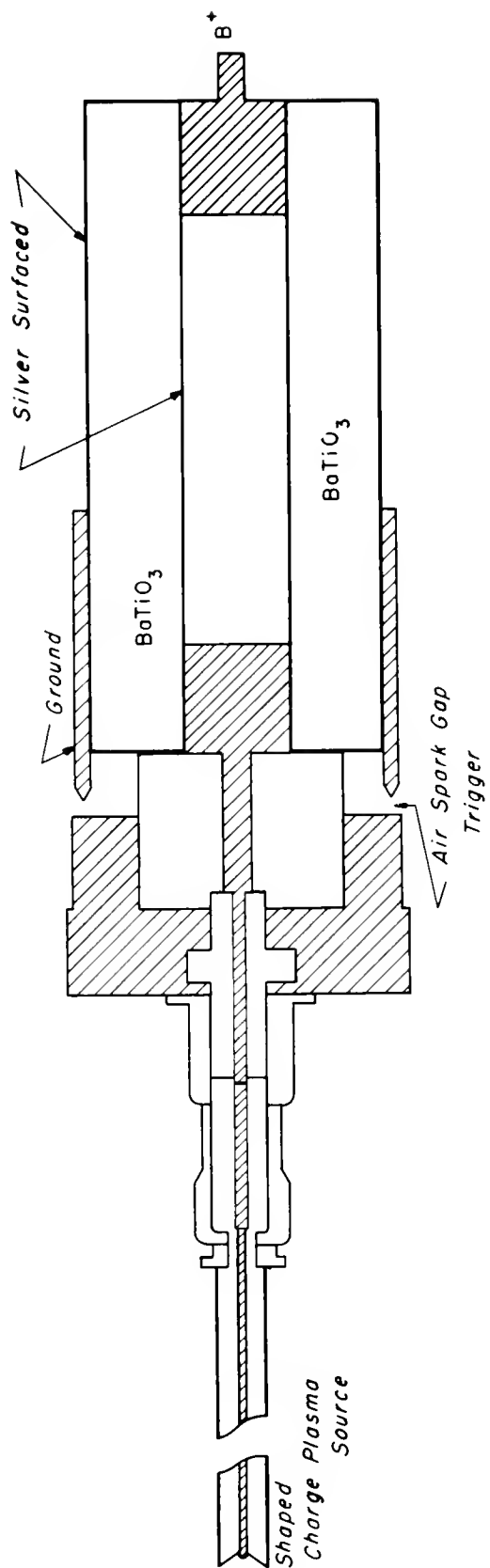


Figure 30  
Detail of Spark Gap Trigger





## APPENDIX IV

### Laboratory Designed Circuits

There are two circuits to be distinguished; the pulse amplifier, and the main power supply and firing system for the capacitor bank and solenoid.

A rather simple pulse amplifier was designed to magnify the signal from the pulse generator (see Appendix I) to an amplitude sufficient to trigger the air gap of the barium titanate capacitor employed with the plasma trigger (see Appendix III). The circuit is shown in Figure 31. It was found that a 20 V trigger satisfactorily tripped the 2D21 at about -12 V bias. The resulting +200 V swing was adequate to trigger the 5C22.

The main power supply for charging the capacitor bank is shown in Figure 32. The plate transformer was a 6 kVA commercial item (United Transformer, Model CG-309), operated on two phase (208 V) with one leg direct and one fed through a motor driven 2.8 kVA variable transformer (Powerstat Model MB 136). Rectification was provided by a mercury vapor tube bridge. The variable transformer crank-up time was 5 sec. Charging resistance to the bank (840  $\mu$ F, 3 kV) was usually 2000 ohms (500 ohms in ignitron unit).

The ignitron unit is shown in Figure 33. The GL 5550 and the GL 7171 have maximum pulse current ratings of 900 amps and 30,000 amps, respectively. The former is shown here triggering the latter at 3 kV and 200 amps. The trigger for the GL 5550 was taken from the discharge of 20  $\mu$ F at 600 V, as shown, the

capacitors being charged by a variable voltage divider, off  $B^+$ , that could be adjusted to compensate for various desired firing voltages on the main capacitor bank (the circuit is shown here adjusted for 3 kV). The 0.001  $\mu\text{F}$ , 10  $\mu\text{F}$ , and 0.1  $\mu\text{F}$  capacitors were employed for noise suppression. The one megohm voltage divider circuit off the ignitor was used occasionally as an oscilloscope trigger. The label "coil" refers to the main solenoid to be energized. The 10K resistance was employed to protect the bank from isolation. Buzzer and bell were warnings of "ready" and "charging".

The control unit for the charging and firing system is shown in Figure 34. This unit was designed to perform the following functions: provide filament and control power and time delay for the filaments, protect against the variable transformer drive motor being in the off-zero position or lacking activating power, provide a signal for activating the main power supply to begin the bank charging cycle, provide a voltmeter sensing unit (meter relay circuit) for deactivating the power supply and firing the ignitron unit at a pre-set voltage, provide means for immediate (or emergency) firing of the ignitron unit at any stage of the charging cycle (if the voltage is too low, the ignitron will not fire and the bank will discharge through the 10K resistor), and provide primary current monitoring on one input leg of the power supply. There are also provisions for stopping the drive motor of the variable transformer at any time after initiation of the charge-fire cycle, and for extinguishing all console and indicator lights.















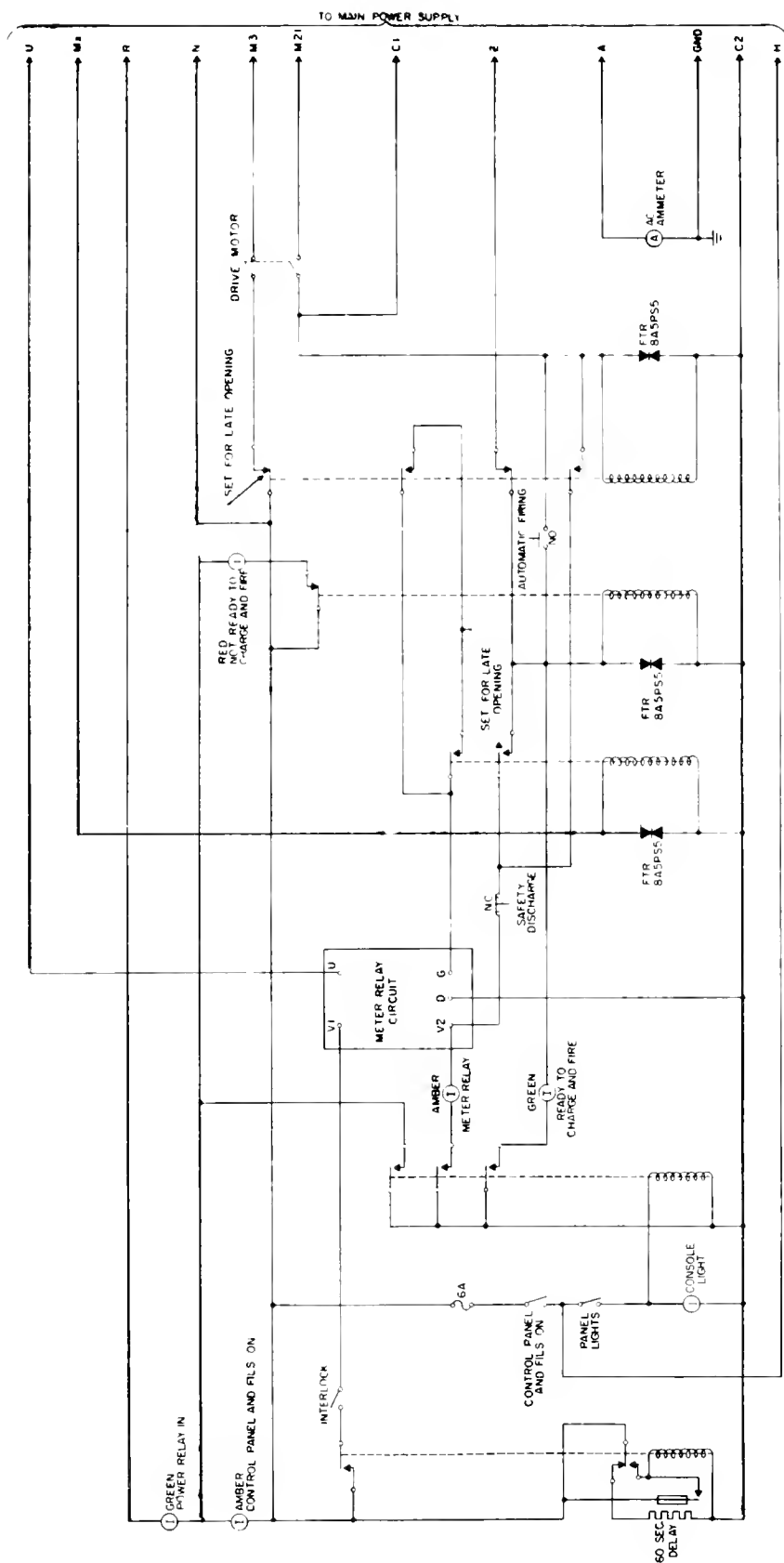


Figure 34  
Control Unit Circuit



Details of the meter relay circuit are shown in Figure 35. It is seen that the V1-V2 circuit is not closed unless the DC circuit for powering the relay is operative (i.e., fail-safe). The reversing switch compensates for change in bank polarity. The "meter hold" switch is usually left open so that appropriate relays in the control unit can release the meter (which is of the "locking" variety) after firing.

## APPENDIX V

### Photomultiplier Experiment

The center-of-mass and thermal velocity results were obtained from oscilloscope traces of photomultiplier (PM) outputs, the PM assemblies being stationed at three positions along the experiment tube, as described in Section IIG.

Each assembly consisted of a 6292 PM (Tracerlab Model RLD-2 Gamma Scintillation Spectrometer Detector with the sodium iodide crystal removed), powered at -2500 V (Tracerlab Model RLS-1). A three foot collimating tube was attached to the front of the PM with a thin slit in the cover at the far end, which was oriented normal to the experiment axis. Thus, the error in position at each PM station was of the order of one millimeter. The sensitivity of the 6292 is extremely large; consequently, several neutral density filters were required for each assembly, in some cases, reducing the maximum light intensity by four to six orders of magnitude in order that the tube not be overdriven. The outputs of the three PM assemblies were each run to ground through an appropriate dropping resistor, the potentials developed being read on separate oscilloscopes (Tektronix, Model 545, with Type 53/54K Plug-In Preamplifier). Dropping resistances were in the range of 500 to 1000 ohms, with current maxima of 0.3 to 3 mA.

Oscilloscope triggering was arranged in the following fashion. Time zero was taken to be the firing of the trigger spark gap on the main plasma source. A 929 phototube was focused on the gap;

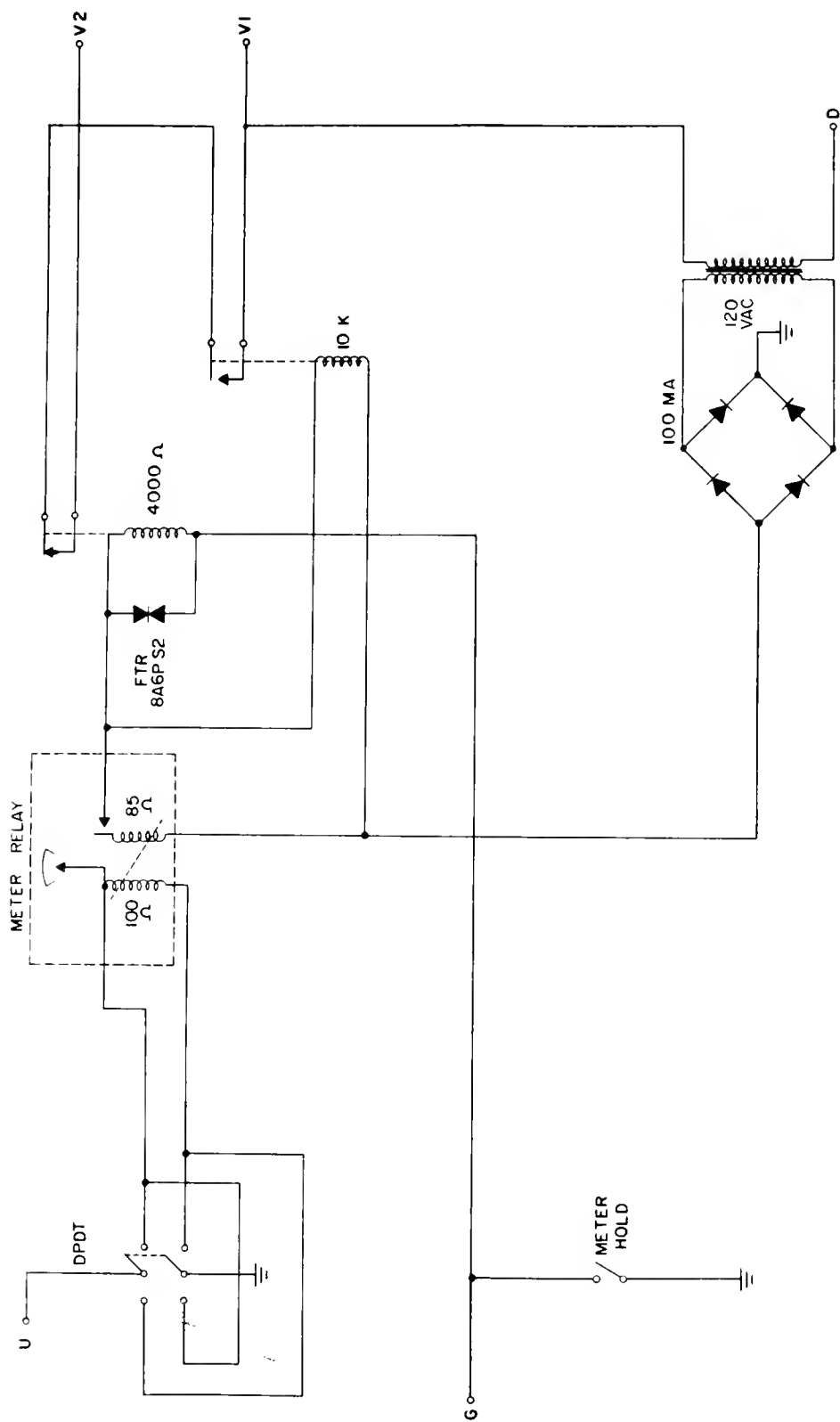


Figure 35



the emitter was kept at -300 V by a regulated power supply while the anode was taken to ground through an appropriate dropping resistance. The potential developed (negative) triggered the first oscilloscope (the PM assembly closest to the plasma source). A rather curious fact emerged in connection with designing this arrangement. If the plasma source was fired without the main confining field being activated (the beginning of the solenoid was a foot or more above the spark gap) the light from the spark gap produced a triggering signal of approximately -10 V across 350 ohms. If the main solenoid was activated also (and was therefore at maximum field when the spark gap was energized) the spark gap light was considerably diminished; a dropping resistance of 3900 ohms was required to develop a satisfactory triggering potential.

The second oscilloscope was triggered from the positive gate of the first, and the third from that of the second. It was established that each gate introduced a delay of approximately 0.1  $\mu$ sec. The sweep times of the three oscilloscopes had been synchronized on the sweep scales actually employed.

## APPENDIX VI

### Determination of Flux Distribution in Multiple Circular Coils with Axial Symmetry

In Section IIE1 it was indicated that a circular model with axial symmetry could be employed to approximate the helical windings (Differential Solenoid) employed in this experiment. The procedure consists, first, of approximating each turn by a circular filament and reducing the model to two dimensions. Then the field created by the filament is obtained for any position on the plane, and thus in space, as a function of the current in the filament, by application of the Biot-Savart law (actually, one obtains  $B_r$ ,  $B_z$ , and  $\Phi/2\pi$ , a stream function). If there are many turns, then the effect of all the filaments on the point in question must be summed.

Once the results are obtained for the first point in the  $(r \geq 0, z)$  half-plane, one can then move in the  $z$  (axial) direction a small, convenient distance and then proceed to search in the radial direction for another point of the same stream-function magnitude. Having found the point,  $B_r$  and  $B_z$  can be computed again and the process continued. In this way, by choosing various starting positions for streamlines, the entire field can be mapped to any desired degree of completeness.

It may be seen that this procedure has wide applicability. Consider a coil with varying spacing between turns and varying radius, or a group of coils in which, in addition, the current is altered. If cylindrical symmetry obtains, the model is applicable. Even more complex is the single turn of heavy copper,



perhaps machined in such a way as to alter the current distribution, which is particularly popular in some "mirror machine" designs. By dividing the cross-section of the turn into individual filaments with appropriate currents, the model results. The accuracy of the model is improved by increasing the number of subdivisions.

This problem is ideal for digital machine computation and was Fortran-programmed for the IBM 704. Input consisted of the coordinates of the intersection of each filament with the r-z half-plane, together with the current, and the coordinates of one or more starting positions of streamlines. One specified also the length of the jump in both the z and r directions for searching the next point, the degree of permitted error in the magnitude of the stream function, and a maximum r and z as cut-off for each streamline. There was provision for relocating a given streamline further down the axis which may have become cut off in r as a result of a gap in the coil winding.

For those who may desire to employ this code, located at the Institute, it is identified as NYU 22.7. Input symbols are: C, current in a current filament; PSI, the stream function magnitude, equal to  $\bar{\Phi} / 2\pi$ ; RHO, the radial location of the intersection of a current filament in the half-plane; ZETA, the axial location of a current filament; RS, the starting radial position for the plot of a streamline at the first axial value of ZS; ZS, the starting axial position for the plot of a streamline and any subsequent axial position at which it is to be relocated; NCOIL, the number of current filaments being employed

in the model; NLINE, the number of streamlines to be plotted; NPOSN, the number of additional axial positions (ZS), plus one, for which streamlines already requested are to be relocated (assuming that some streamlines have been cut off by having acquired too large a radial component; if a streamline was not cut off then the machine will ignore the order to recompute it at the new ZS); RT, the radial dimension at each value of ZS beyond which the machine will not attempt to relocate a streamline; H, the trial step in the axial direction for locating the next point on the same streamline; DR, the trial step in the radial direction (after having moved H) for locating a point the streamline magnitude of which will differ from the previous point an amount less than ERROR; ZMIN, ZMAX, line-plot cut-offs in the axial direction; RMAX, same for the radial direction.

In the printed output each page (or group of pages) will contain the data for one streamline, headed by its magnitude, and including every point on the line, together with the values, for that point, of the magnetic field intensity (B) and its radial and axial components (BR, BZ). The numerical answers are given in field intensity, not induction (despite the use of "B"), and if linear dimensions are given in meters and current in amperes, the results will be unrationalized MKS (i.e.,  $\mu_0 = 10^{-7}$ ). Similarly,  $\Phi = 2\pi\mu_0 \text{PSI}$ .

There are some words of caution appropriate to this machine code. As was previously noted, the model becomes decreasingly applicable in regions close to the current sheath (i.e., the coils) if the actual winding involves helical rather than cylindrical

symmetry. Also, in obtaining line plots close to coils, small test jumps are recommended, of magnitude significantly smaller than the distance to the nearest coil (filament), else the machine will become "lost" and not find the next point. Since the mathematical expressions employed involve elliptic integrals, care must be taken in this region (near the coils) that the machine sub-routine for the integral is employing a sufficient number of terms (or that there is some alternate provision), as a modulus close to unity (which is the result of a close approach to a filament) produces an approach to infinity in integrals of the first kind. Finally, note that the value of B on the axis may not be obtained since the stream function is zero there and, thus, smaller than the smallest permissible error (in fact, the program will skip such a request).



## REFERENCES

1. D. Finkelstein, M. Ehrlich, I. Livingston, and D. Wetstone, "Experiments on Supersonic Plasma Flow Along Magnetic Fields", AEC NYO Report No. 7981, March 27, 1958.
2. A summary of these approaches is given by A. Simon, An Introduction to Thermonuclear Research, Pergamon Press, New York, 1959, and detailed descriptions of current work are contained in Proceedings of the Second United Nations International Conference on the Peaceful Uses of Atomic Energy, United Nations, Geneva, 1958, Sessions 4, A-5, A-6, A-7, A-9, and A-10.
3. W. Bostick, Phys. Rev. 104, 292 (1956); *ibid.*, 106, 404 (1957).
4. W. Bostick, Astrophys. J. 127, 237 (1958).
5. D. Finkelstein, G. A. Sawyer, and T. F. Stratton, Phys. Fluids 1, 188 (1958).
6. K. D. Sinelnikov, *et al.*, Proceedings of the Second United Nations International Conference on the Peaceful Uses of Atomic Energy, United Nations, Geneva, 1958, Session A-6, Paper P/2536.
7. F. H. Coensgen, W. F. Cummins, and A. E. Sherman, Phys. Fluids 2, 350 (1959).
8. J. Marshall, Proceedings of the Second United Nations International Conference on the Peaceful Uses of Atomic Energy, United Nations, Geneva, 1958, Session A-6, Paper P/355.
9. E. R. Harrison and R. H. Dawton, J. Electronics and Control 5, 29 (1958).
10. H. Edels, British Electrical and Allied Industries Research Association, Technical Report L/T230 (1950).



11. W. S. Boyle, P. Kisliuk, and L. G. Germer, J. Appl. Phys. 26, 720 (1955).
12. C. G. Suits, G. E. Review 39, 194 (1936).
13. J. M. Meeks and J. O. Craggs, Electrical Breakdown of Gases, Clarendon Press, Oxford, 1953, Chap. X.
14. H. S. W. Massey, Handbuch der Physik, (edited by S. Flügge), Springer-Verlag, Berlin, 1956, Vol. 36, p. 307.
15. L. Spitzer, Physics of Fully Ionized Gases, Interscience Publishers, New York, 1956.
16. G. Elwert, Z. Naturforsch. 7a, 432 (1952).
17. G. Knorr, Z. Naturforsch. 13a, 941 (1958).
18. R. Courant and K. O. Friedrichs, Supersonic Flow and Shock Waves, Interscience Publishers, New York, 1948, p. 155.
19. D. Bohm, E. H. S. Burhop, and H. S. W. Massey, The Characteristics of Electrical Discharges in Magnetic Fields, (edited by A. Guthrie and R. K. Wakerling), McGraw-Hill Book Co., New York, 1949, p. 65.
20. A. Simon, Proceedings of the Second United Nations International Conference on the Peaceful Uses of Atomic Energy, United Nations, Geneva, 1958, Session A-10, Paper P/366.
21. B. Lehnert, *ibid.*, Session A-10, Paper P/146.
22. For example, see the discussion in R. F. Post, Rev. Mod. Phys. 28, 338 (1956).

[illegible]

46

PRINTED IN U. S. A.



NYU

NYU-

2577 Wetstone.

c. 2 Experiments in super-  
sonic plasma flow along  
magnetic fields. II.

NYU

NYU-

2577 Wetstone.

c. 2

Experiments in super-  
sonic plasma flow along  
magnetic fields. II.

**N. Y. U. Institute of  
Mathematical Sciences**

25 Waverly Place  
New York 3, N. Y.

